

# Pressure-induced and flaring photocatalytic diversity of ZnO particles hallmarked by finely tuned pathways

Martina Vrankić,<sup>a,\*</sup> Ankica Šarić,<sup>a,\*</sup> Takeshi Nakagawa,<sup>b</sup> Yang Ding,<sup>b</sup> Ines Despotović,<sup>c</sup> Lidija Kanižaj,<sup>d</sup> Hirofumi Ishii,<sup>e</sup> Nozomu Hiraoka,<sup>e</sup> Goran Dražić,<sup>f</sup> Dirk Lützenkirchen-Hecht,<sup>g</sup> Robert Peter<sup>h</sup> and Mladen Petravić<sup>h</sup>

<sup>a</sup>*Division of Materials Physics and Center of Excellence for Advanced Materials and Sensing Devices, RuđerBošković Institute, Bijenička 54, 10000 Zagreb, Croatia.* [mvrankic@irb.hr](mailto:mvrankic@irb.hr), [Ankica.Saric@irb.hr](mailto:Ankica.Saric@irb.hr)

<sup>b</sup>*Center for High-Pressure Science & Technology Advanced Research, 100094 Beijing, P.R. China.* [takeshi.nakagawa@hpstar.ac.cn](mailto:takeshi.nakagawa@hpstar.ac.cn), [yang.ding@hpstar.ac.cn](mailto:yang.ding@hpstar.ac.cn)

<sup>c</sup>*Division of Physical Chemistry, Ruđer Bošković Institute, 10000 Zagreb, Croatia.* [Ines.Despotovic@irb.hr](mailto:Ines.Despotovic@irb.hr)

<sup>d</sup>*Division of Materials Chemistry, RuđerBošković Institute, 10000 Zagreb, Croatia.* [Lidija.Kanizaj@irb.hr](mailto:Lidija.Kanizaj@irb.hr)

<sup>e</sup>*National Synchrotron Radiation Research Center, Hsinchu 30076, Taiwan.* [h\\_ishii@spring8.or.jp](mailto:h_ishii@spring8.or.jp), [hiraoka@spring8.or.jp](mailto:hiraoka@spring8.or.jp)

<sup>f</sup>*Department of Materials Chemistry, National Institute of Chemistry, Hajdrihova 19, Ljubljana, Slovenia.* [goran.drazic@gmail.com](mailto:goran.drazic@gmail.com)

<sup>g</sup>*Fk. 4, Physik, Bergische Universität Wuppertal, Gauss-Straße 20, D-42097 Wuppertal, Germany.* [dirklh@uni-wuppertal.de](mailto:dirklh@uni-wuppertal.de)

<sup>h</sup>*University of Rijeka, Department of Physics and Centre for Micro- and Nanosciences and Technologies, RadmileMatejčić 2, 51000 Rijeka, Croatia.* [robertpeter@phy.uniri.hr](mailto:robertpeter@phy.uniri.hr), [mpetravic@phy.uniri.hr](mailto:mpetravic@phy.uniri.hr)

Corresponding authors at: Division of Materials Physics and Center of Excellence for Advanced Materials and Sensing Devices, RuđerBošković Institute, Bijenička 54, 10000 Zagreb, Croatia.  
*E-mail address:* [mvrankic@irb.hr](mailto:mvrankic@irb.hr) (Martina Vrankić), [Ankica.Saric@irb.hr](mailto:Ankica.Saric@irb.hr) (Ankica Šarić)  
Phone: +385 1456 1120

## Abstract

Microstructure and morphology of particles play key roles in optimizing the properties of shape-selected ZnO particles, which are essential factors for flexible and reliable applications. In particular, chemical understanding and physical measurement with scientific theory must be further integrated for the realization of finely tuned ZnO nano/microstructures with desired sizes and shapes. Herein, we deliver a detailed description of the mechanism that mimics the formation of finely-tuned, spherical ZnO nanoparticles (NPs) at the computational level. We tackled issues that significantly affect the favorable structural motifs of the spherical ZnO NPs grown hydrothermally from ethanolic solution leading to their advancing chemical and physical properties. The excellent photocatalytic activity of the spherical ZnO was addressed by an apparent-rate constant of  $9.7(2) \times 10^{-2} \text{ min}^{-1}$  efficiently degrading the Rhodamine B solution by ~99 % in 50 min. The apparent-rate constant for tubular ZnO particles is almost six times lower than that of spherical ZnO NPs. Comparative results revealed that the diversity of size and shape of ZnO particles distinguishes the wurtzite-to-rocksalt transformation reversibility phenomena by dictating the microstructure-dependent deformation behavior and ultimately leading to different transition-induced elastic strain responses to hydrostatic pressure up to 30 GPa.

**Keywords:** high pressure; X-ray diffraction; microstructure; phase transition; oxide materials; catalysis

## 1. Introduction

Topping advancements in ZnO-based nanotechnology over the last decades have significantly raised the interest for the cost-effective fabrication of functionalized ZnO-based materials[1–6]. A powerful combination of unique optical, semiconducting, piezoelectric, and catalytic properties[7,8] fused with thermal and chemical stability[9], as well as both biocompatible and biodegradable peculiarities[10] leads to superior functionality[11,12, 13] of ZnO-based nanomaterials. Due to a wide bandgap and high electron mobility, ZnO is frequently used as an electron extracted layer in the perovskite-based solar cell, whereas the performances of photodetector can be significantly improved[14–18]. Namely, the ZnO can passivate the perovskite and eliminate trap states on its surface and grain boundaries, which contributes to the superior sensing properties with high and fast response. At the same time, the ZnO NPs, which

occur, in a wide range of morphologies[19], have been rediscovered as innovative agents for medical applications[20]. In their 2020 outlook, Wiesmann, Tremel, and Briegera outlined a breakthrough role of ZnO NPs as pioneering anti-tumor agents in cancer medicine[21]. Based on their great prerequisites, several research groups[22,23], reported the successful binding of ZnO NPs with the COVID-19 targets, *via* the formation of hydrogen bonds, and highlighting the competence of the ZnO NPs strongly related to the effects of microstructure and morphology. Given the rising importance of ZnO-based applications, defining and establishing the most optimal preparation route of functionalized ZnO-based materials have become an essential matter to be dealt. Although significant superiority and better performance of ZnO NPs over other antiviral metal oxides NPs[24–26] has been shown, their rather poor application in the photodegradation processes of dye pollutants, such as Rhodamine B (RhB,  $C_{28}H_{31}ClN_2O_3$ ) and/or Methylene Blue (MB,  $C_{16}H_{18}N_3SC$ ), limits a large-scale application. Namely, the low-cost and chemically stable semiconductors such as  $TiO_2$ , ZnO, and  $SnO_2$  have relatively large band gaps and mainly absorb UV photons only [27,28]. However, these narrow bandgap materials are rather poorly used in photocatalysis due to higher fabrication costs and chemical instability. In particular, the main barriers for effective ZnO applicability are the narrow light-absorption range, the photoinduced corrosion–dissolution at extreme pH conditions, the charge-carrier recombination, and the formation of inert  $Zn(OH)_2$  during photocatalytic reactions. To overcome these barriers, metal and non-metal doping, morphology control, and sensitization with optical and plasmonic nanostructures are often used to extend the absorption range of the ZnO photocatalyst. Particularly, the upconversion nanomaterials can serve as a frequency converter, i.e. convert two or more NIR photons to visible or UV photons, where converted photons can be reabsorbed by photocatalysts leading to their efficiency improvement [29]. Additionally, the surface plasmonic resonance photocatalysts composed of noble metal NPs deposited on the surface of semiconductor materials have recently shown promising results towards the visible-light-driven photocatalysis, where metal NPs act as sensitizers for harvesting visible light due to their surface plasmon resonance and the metal-semiconductor interface efficiently separates the photo-generated charges [30–32]. Bora et al. showed that localized plasmonic heating has a crucial role in defining the efficacy of the Au-ZnO-based plasmonic photocatalysts apart from their higher visible light harvesting and improved charge separation across the metal-semiconductor interface [33]. As a result of the plasmonic effects from Au NPs the activation

energy required for the photocatalytic degradation of Methylene blue dye pollutant was reduced by 22.5 % in the presence of the Au NPs, which demonstrated visible light photocatalytic activity almost double than the bare ZnO nanorods under the solar light irradiation. Indeed, the main drawback of the efficient photocatalytic activity of ZnO and the enhanced quantum yield is manifested in a very small apparent first-rate constant,  $k_{app}$ , due to the rapid recombination of photogenerated electrons and holes[34,35]. A recent review by Pirashemi et al. (2015) reported that the degradation rate constants of RhB dye over the ZnO and ZnO/Ag<sub>2</sub>CrO<sub>4</sub> catalysts are  $13.3 \times 10^{-4}$  and  $213 \times 10^{-4} \text{ min}^{-1}$ , respectively. Thus, the activity of the ZnO/Ag<sub>2</sub>CrO<sub>4</sub> nanocomposite was about 16 times larger than that of pure ZnO[36]. Neena and co-workers (2018) published the value of the rate constant of  $9.16 \times 10^{-4} \text{ min}^{-1}$  for the Fe-Cd co-modified ZnO over RhB dye solution, which is  $\sim 3.7$  times higher than that of pure ZnO[37]. Recent findings, by Ma et al. (2021), estimated from the photocatalytic degradation kinetics of pure ZnO and Ar-H plasma-modified ZnO catalysts over RhB dye pollutant, highlighted a degradation rate of Ar-H plasma-modified ZnO, 20 times greater than that of pure ZnO, with  $k_{app}$  values of  $8.933 \times 10^{-2} \text{ min}^{-1}$  for Ar-H plasma-modified ZnO and only  $3.96 \times 10^{-3} \text{ min}^{-1}$  for pure ZnO[38].

Interestingly, there has been no report on the synthesis of pure ZnO photocatalyst with highly efficient photodegradation activity, despite extensive attempts in this field. Chemically, the surface of ZnO NPs is rich in -OH groups, which can be easily decorated and functionalized by various surface decorating molecules[39,40]. It is important to note that the reactivity of ZnO NPs in most applications arises from their interaction with an aqueous medium. However, a thorough understanding of the interaction of ZnO NPs with H<sub>2</sub>O at the atomic level is still lacking. The large affinity of H<sub>2</sub>O molecules for ZnO NPs leading to the spontaneous dissociation of H<sub>2</sub>O was demonstrated by the Petridis group[41]. Šarić et al. reported a strong influence of the synthesis route on the formation of ZnO NPs, their size, and geometrical shape in several recent papers[42–46].

Addressing both chemical and physical properties (i.e. high-pressure experimental data on strain/stress, crystallite size, and shape) of these highly attractive ZnO NPs with exceptional semiconducting, piezoelectric, and pyroelectric properties is extremely important for further implementation in various industries. Elucidating the effects of both, microstructure[47] and morphology[48–50] on the properties of ZnO under high pressure is a foundation for exploring

the physical and chemical mechanisms that govern the intertwined structure–property relationships. The structure of ZnO at ambient conditions adopts the space group symmetry  $P6_3mc$  ( $a=3.25224(7)$  Å,  $c=5.20955(12)$  Å,  $V=47.72$  Å<sup>3</sup>)[51] consisting of two interpenetrating hexagonal-closed-packed (hcp) sublattices (i.e. wurtzite structure,  $w$ ) and can be driven by external hydrostatic pressure into a cubic arrangement (i.e. rock salt structure,  $rs$ ) with  $F-43m$  space group setup ( $a=4.489$  Å,  $V=90.46$  Å<sup>3</sup>)[52]. The pressure-induced hexagonal to cubic phase transition in ZnO occurs at a relatively modest pressure of  $\sim 10$  GPa and is accompanied by a large volume decrease of about 17 %, as reported by Bates et al. in their seminal 1962 study[53]. Much work has been done on the high-pressure behavior of the bulk ZnO along with the structural stability and reversibility of the phase transition processes[54–60], but there are still some critical obstacles that need to be elucidated, both experimentally and theoretically. In particular, the establishment of the methodology to physically control the reversibility of the  $w$  to  $rs$  phase transition by external pressure stimuli and the direct construction of shape-selected ZnO NPs, i.e. morphology-controlled ZnO synthesis routes, by developing the theoretical mechanisms that can control the specific functionality, remain to be elucidated.

This work takes a fresh look at the physical and chemical peculiarities of shape-selected ZnO particles prepared by different routes, concisely elaborating the mechanical response to external hydrostatic pressure via Synchrotron Powder X-ray diffraction (SPXRD) experiments and the enhanced degradation kinetics over RhB dye pollutant. The characterization panorama is further implemented with results from Transmission Electron Microscope (TEM) and Scanning Electron Microscope (SEM) micrographs and X-ray Photoelectron Spectroscopy (XPS) fingerprints, which provide a detailed insight into the morphological versatility and surface diversity of synthesized ZnO polycrystals. The impact of morphologically tuned nano- and micro-sized ZnO particles on photocatalytic activity is evaluated through the energy bandgap calculations from UV-Vis absorption spectra. Herein, we have mimicked theoretical breakthroughs at the Density Functional Theory (DFT) level leading to morphology-driven ZnO NPs, reflecting enhanced catalytic activity and pressure-induced internal strain contributions to the mechanical properties of nanocrystalline ZnO particles.

## **2. Experimental**

### *2.1 Materials and Synthesis*

Zinc acetylacetonate monohydrate [ $\text{Zn}(\text{C}_5\text{H}_7\text{O}_2)_2 \cdot \text{H}_2\text{O}$  Alfa Aesar 96%, Germany], sodium hydroxide (NaOH; Kemika reagent grade 98%; Croatia), triethanolamine ( $\text{C}_6\text{H}_{15}\text{NO}_3$ ; Fisher Chemical p.a. 99.5%, USA), absolute ethanol ( $\text{CH}_3\text{CH}_2\text{OH}$ ; J. T. Baker 99.9%; Netherlands), and 1-octanol [ $(\text{CH}_3(\text{CH}_2)_7\text{OH}$ ; Sigma Aldrich reagent grade 99%, Germany], were used to prepare the samples. Double distilled water was prepared in our laboratory. Hydrothermal syntheses of ZnO NPs were carried out in the presence of triethanolamine (TEA) using  $\text{CH}_3\text{CH}_2\text{OH}$  and  $\text{CH}_3(\text{CH}_2)_7\text{O}$  following the procedure described in more detail in ref. [43]. Specifically, sample S1 was synthesized by adding  $\text{Zn}(\text{acac})_2 \cdot \text{H}_2\text{O}$  (0.5 g) to the ethanolic solution of TEA (30 ml) and adjusting the molar ratio TEA/ $\text{Zn}(\text{acac})_2 \cdot \text{H}_2\text{O}$  to 1:2. Similarly, the TEA/octanol precursor solution for the synthesis of sample S2 was prepared using  $\text{CH}_3(\text{CH}_2)_7\text{OH}$ , with the molar ratio of TEA to  $\text{Zn}(\text{acac})_2 \cdot \text{H}_2\text{O}$  being 1:1. The prepared transparent precursor solutions were autoclaved at 170 °C for 72 h, using 50 mL Teflon-lined stainless steel autoclaves. After autoclaving, the obtained precipitates were centrifuged in one step, washed several times with ethanol, and dried overnight in vacuo at room temperature (RT). A typical synthesis of the sample T1 involved dissolving a defined amount of  $\text{Zn}(\text{acac})_2 \cdot \text{H}_2\text{O}$  (2.0 g) in an aqueous NaOH solution (200 ml) according to the procedure described in [42]. The transparent precursor solution was autoclaved for 24 h at 90 °C. The obtained precipitates were separated from the supernatant using a centrifuge, additionally rinsed with ethanol and Milli-Q water, and finally dried at 110 °C. The product obtained was heated to 300 °C in an oven with still air at a heating rate of 10 °C/min, and finally calcined at this temperature for 4 h.

## 2.2 Fourier-transform infrared (FTIR) spectroscopy.

The surfaces of the ZnO particles were investigated by FTIR to determine the presence of the characteristic stretching vibrations. The infrared spectra were recorded in the 4000–200  $\text{cm}^{-1}$  region with samples as KBr pellets using a Perkin-Elmer Model 2000 spectrometer.

## 2.3 Powder X-ray diffraction (PXRD) measurements at ambient conditions

PXRD measurements at RT were collected in reflection mode using a monochromatic Cu  $K\alpha$  X-ray source ( $\lambda = 1.54056 \text{ \AA}$ ) on a Philips PW1880 diffractometer with a step size of  $0.02^\circ$  in the  $2\theta$  range between  $10^\circ$  and  $70^\circ$ .

#### 2.4 *In-situ SPXRD experiments at non-ambient conditions*

The *in situ* SPXRD experiments were performed on the Taiwanese BL12B2 sector of SPring-8 facility (Hyogo, Japan). Two wide-opening Diamond Anvil Cells (DACs) with 4 pins and shallow DAC with 3 pins were prepared for pressurization with diamond anvils of 400  $\mu\text{m}$  culet diameter. Each finely ground powder sample was compressed into a small pellet and loaded along with a ruby sphere into a stainless steel gasket of defined pre-pressed thickness and drilled hole. SPXRD measurements were collected at RT in axial geometry. Details are summarized in the Supplementary Information. Silicone oil was used as the pressure-transmitting medium and each pressure point was determined by the matching pressure shift of the ruby fluorescence line[61]. A monochromatic X-ray beam with a wavelength of  $0.5657 \text{ \AA}$  was used as the probe source. The sample-detector distance and other parameters of the detector were calibrated using the  $\text{CeO}_2$  standard. Diffraction patterns were recorded using a Charge-Coupled Device (CCD) image plate detector ( $0.073 \times 0.073 \text{ mm/pixel}$ ). Two-dimensional diffraction patterns were integrated into one-dimensional profiles with an IPAnalyzer and peak positions were determined semi-automatically with PDIndexer software[62].

Structure refinements against one-dimensional diffraction data were performed with the Rietveld algorithm[63] using the X'Pert HighScore Plus program[64]. A pseudo-Voigt profile function and a polynomial background with up to six coefficients were applied to the structure refinements. Crystallite size and lattice microstrain information were extracted from the phase fitting method (i.e. simultaneously with the Rietveld structure refinements) based on the change in profile widths compared to a standard sample. The tensor surfaces were additionally evaluated and interpreted using a generalized model for the broadening of microstrain peaks within the GSAS II software[65]. Quantitative phase analysis was performed using the formalism described by Hill and Howard[66]. For each phase, all compression data points were fitted with the third-order Birch-Murnaghan Equation of State (EOS)[67] using EosFit7 software[68]. A realistic estimate of the compression parameters is given by the following formula:

$$p = \frac{3}{2} B_0 \left[ \left( \frac{V_0}{V} \right)^{\frac{7}{3}} - \left( \frac{V_0}{V} \right)^{\frac{5}{3}} \right] \left\{ \mathbf{1} - \frac{3}{4} (4 - B'_0) \times \left[ \left( \frac{V}{V_0} \right)^{\frac{3}{4}} - \mathbf{1} \right] \right\} \quad (1)$$

where  $B_0$  is isothermal bulk modulus at atmospheric pressure,  $B'_0$  is its pressure derivative ( $\equiv dB_0/dP$ ), and  $V_0$  is the unit cell volume at zero pressure.

## 2.5 Surface morphology imaging

Morphological analysis was performed using a Field Emission Scanning Electron Microscope (FE-SEM) JSM-7000F and a Cs-corrected probe Cold Field Emission (CFE) Scanning Transmission Electron Microscope (STEM) Jeol ARM 200 CF. A low beam current and electron energy of 80 keV were used to minimize the beam damage. High-Angle Annular Dark-Field (HAADF) images were acquired using 68-180 mrad collection half-angles at 24 mrad probe convergence semi-angles. The Gatan Quantum ER dual Electron Energy-Loss Spectroscopy (EELS) and JeolCenturio Energy Dispersive X-ray Spectroscopy (EDXS) system with 100 mm<sup>2</sup> Silicon Drifted Detector (SDD) were used for chemical analysis. The powder samples were directly transferred to the lacey carbon-coated nickel STEM grids.

## 2.6 The Brunauer–Emmett–Teller (BET) measurements

The specific surface area of the powders was analyzed by nitrogen adsorption using a Micrometrics' Gemini surface area analyzer.

## 2.7 Photocatalytic activity measurements

Photocatalytic activity of the samples was monitored by photodegradation of aqueous RhB dye under ultraviolet (UV) light. For each reaction, 3 mg of the powder sample was dispersed in a 3.0 ml of 10 ppm aqueous RhB dye solution. Before irradiation with UV light, the suspension was sonicated for 5 min and stirred constantly for 1 h in the dark to achieve adsorption–desorption equilibrium between the dye solution and the photocatalyst. Then, eight UV lamps of 352 nm (8 watt, Hitachi) were turned on to start photodegradation in a photoreactor (Luzchem LZC-4V). A magnetic stirrer was placed at the bottom of the cell containing the reaction mixture to maintain homogeneity. After the suspension was kept under UV light irradiation, a certain amount of the sample (2 mL) was taken at fixed time intervals (20 min) and centrifuged at 7000 rpm for 8 min. Photocatalytic degradation reactions were monitored by



measuring the concentration of a degraded supernatant liquid as a function of irradiation time by UV-Visible (UV-Vis) absorption spectra using a UV-Vis spectrophotometer (Varian Cary 50). Blank experiments were performed without the photocatalysts. The extracted information from the RhB dye solution photocatalytic degradation curves allowed the determination of the reaction type and the calculation of the kinetic constant of the RhB pollutant solution degradation reaction. All experiments were conducted at RT at pH=7. The degradation rate  $r$  of the RhB dye solution can be expressed as[69]:

$$r = -d(C)/dt = k_{app}(C)^n \quad (2)$$

where  $C$  is the concentration of RhB pollutant molecules,  $k_{app}$  is the apparent-rate constant and  $n$  is the order of the reaction. The absorbance at 554 nm was used to calculate the amount of RhB dye solution that degraded with time. The percentage of degradation was calculated using the following formula[70]:

$$\text{Degradation \%} = [(C_0 - C_t)/C_0] \times 100 \quad (3)$$

where  $C_0$  and  $C_t$  are the initial concentration and the concentration after exposure to UV light at time  $t$ , respectively. The  $k_{app}$  was calculated using the slope of the graph of  $\ln C_0/C_t$  versus the irradiation time. To explore the reusability of the optimal sample, after separating it *via* centrifugation from the reaction mixture, the recovered catalyst was used with fresh RhB solution. Namely, after the reaction, the catalyst from each cycle was thoroughly rinsed several times with ethanol and dried overnight at RT. The recovered catalyst was reused for the degradation of RhB dye each time under identical reaction conditions. The degradation efficiency of the ZnO catalyst was tested within 3 cycles at pH=7, whereas the photocatalytic activity was measured at the end of each cycle.

### 2.8 X-ray photoelectron spectroscopy measurements

The chemical composition of the surface was investigated using a SPECS laboratory XPS system under UHV conditions (the typical pressure was in the range of  $10^{-7}$  Pa) with Al  $K\alpha$  X-rays of 1486.74 eV and the Phoibos100 electron energy analyzer. The pass energy was set to 10 eV, resulting in a total energy resolution of about 0.8 eV. The experimental spectra were fitted with the Gaussian-Lorentzian functions after the Shirley background subtraction[71].

## 2.9 UV-Vis spectroscopy measurements

UV-Vis absorption spectra were recorded using a Shimadzu UV/Vis/NIR Model UV-3600 spectrometer equipped with an integrated sphere. Barium sulfate was used as a reference. The bandgap values were calculated using the procedure described by Tauc and co-workers [72].

## 2.10 Computational methods

Geometry optimizations were performed with quantum chemical calculations at the DFT level using the Gaussian 09 program (revision D1)[73]. The (ZnO)<sub>36</sub> cluster served as a credible model for all possible molecular surface/solvent and surface/TEA additive interaction predictions[74]. Solvent effects (CH<sub>3</sub>CH<sub>2</sub>OH,  $\epsilon=24.85$ ; CH<sub>3</sub>(CH<sub>2</sub>)<sub>7</sub>OH,  $\epsilon=9.86$ ; H<sub>2</sub>O,  $\epsilon=78.36$ ) were accounted for using the implicit Solvation Model Based on Density (SMD) polarizable continuum[75]. The M05-2X functional[76] developed by the Truhlar's group was used. The mixed 6-31+G(d,p) + LANL2DZ basis set was used for geometry optimization, while the Pople's 6-31+G(d,p) double- $\xi$  basis set and LANL2DZ basis[77] were chosen for the H, C, O, N and Zn atoms, respectively. The final single-point energies were refined using a highly flexible 6-311++G(2df,2pd) basis set for the H, C, O, and N atoms, while the same ECP-type LANL2DZ basis set was used for the Zn atoms. Bader's Quantum Theory of Atoms in Molecules (QTAIM)[78] coupled with the AIMALL software package[79] was employed for the topological analysis of electron density. The chemical bond type was qualitatively described by the sign and values of the electron density Laplacian  $\nabla^2\rho(r_c)$  and the electron energy density  $H(r_c)$  at the corresponding bond critical point. The interaction free energies,  $\Delta G^*_{\text{INT}}$ , were calculated as the difference between the total free energy ( $G^*_{\text{AB}}$ ) of the resulting structures and the sum of the total free energies ( $G^*_A + G^*_B$ ) of the associating units.

## 3. Results and discussion

### 3.1 Structural and microstructural response to pressure at room temperature

The resulting white polycrystals of S1, S2, and T1 exhibited single-phase SPXRD patterns at RT and slightly elevated pressures of 0.10 GPa, 0.36 GPa, and 0.50 GPa,

respectively, preserving exclusively the crystal structure of hexagonal pristine *w*-ZnO with  $P6_3mc$  space group symmetry[51] as indicated from the FTIR analysis (see Figs. S1 and S2 and relevant details) and Rietveld refinements (Figs. 1, 2, S3, S4). The resulting unit cell metrics are summarized in Table S1, along with reliability factors that confirm the validity of the refinement. However, when the pressure reached 13.16 GPa, 15.73 GPa, and 12.44 GPa in S1, S2, and T1, respectively (Figs. 1b, 2b, and S3), the *in situ* axial X-ray diffraction (AXRD) profiles revealed the appearance of a new set of reflections not indexed by the hexagonal structural model. The appearance of cubic (111), (020), and (022) Bragg peaks readily confirms the pressure-induced structural phase transition from hexagonal to cubic structure with the  $F\bar{4}3m$  space group assignment[52], which was accompanied by a large volume collapse. As estimated from the Rietveld refinements (Table S1), the mass fraction of the cubic phase increased from 4.0 % at 13.16 GPa to 100 % at 17.68 GPa in the sample S1, a situation that persisted with further pressurization up to 29.40 GPa, the highest pressure applied in the experiments (Fig. 3a). In a remarkably similar fashion, a complete hexagonal to cubic transformation in S2 was achieved by squeezing the sample to 19.50 GPa (inset in Fig. 3a). At 15.73 GPa the mass fraction of the cubic phase in the sample S2 was 36.60 %, apparently continued to increase to 76.40 % at 16.83 GPa and finally up to 100 % at 19.50 GPa. Similarly, the mass fraction of the hexagonal phase fades at 12.44 GPa and kicks into 75.20 % of the cubic fraction in the sample T1. A *w* to *rs* structural transition in S1 completed at  $\sim 17.68$  GPa resulted in a sharp  $\sim 21$  % dip in unit cell volume, while compression of S2 at 19.50 GPa led to the formation of solely cubic phase and  $\sim 20$  % drop in volume, resulting in consequently significant hysteresis. Diversely, a hexagonal to cubic phase transformation was revealed in T1 at 13.77 GPa, mirroring  $\sim 20$  % unit cell volume collapse.

The compressibility plots of the hexagonal and cubic phases of the S1, S2, and T1 samples are shown in Fig. 4, where the transparent solid lines are the third-order fits Birch-Murnaghan EOS[67] to the data for the *w* and *rs* phases. The fits yielded values of the bulk modulus and their pressure derivatives, which are listed in Table 1. The  $B_0$  of the *w* and *rs* phases at zero pressure were estimated to be 141(14) and 130(4) GPa for the samples prepared in alcoholic solutions. These are relatively smaller bulk moduli values compared to the values reported in some previous experiments[58,80] using Si oil as the

pressure medium. Accordingly, the  $B_0$  of the *rs* phase for S1 of 215(3) and 151(2) for S2 correlate favorably with Decramps (2003)[80] and Hanna (2011)[81]. However, since our results for T1 are based on a limited number of pressure points, the results of such analyses should consequently be treated with the utmost caution.

The high pressure phases of both, S1 and S2 were stable up to ~29 GPa. Interestingly, the fingerprints of the cubic diffraction patterns did not reappear during decompression from ~29 GPa to 0 GPa – hexagonal structures were retained beyond the upward transition pressure in both samples, S1 and S2. Such experimental results for the structural transitions in prepared ZnO samples correlate well with data published for bulk ZnO [52,55,81–83] and further support the concept of first-order solid-state transformation in prepared ZnO samples. In contrast, a very different trend was observed for the sample T1 after depressurization (Fig. 2b). Namely, the sample T1 undergoes a first-order pressure-induced phase transformation at 12.44 GPa, followed by the transition zone imaged up to 13.77 GPa and accompanied by a ~20 % volume decrease (Fig. 4). In contrast to S1 and S2, a reversible pressure-induced phase transition to single-phase hexagonal symmetry was observed in the sample T1 by slowly depressurizing from 15.46 GPa to ambient pressure (Figs. 2b and 5). Nevertheless, the phase transitions in all prepared samples followed a two-step hexagonal path[83], which was accompanied by a pronounced linear decrease in the  $c/a$  axis ratio and further led to the formation of the cubic phase. However, it must be emphasized, that being slightly softer along the  $c$ -axis direction[85] even at ambient pressure (i.e. the  $c/a$  axis ratio of 1.6026(6) at 0 GPa, is smaller than the ideal value[86] of 1.633) the hexagonal packing shows a minor indication of an abnormal variation of the  $c/a$  axis ratio near the structural transition pressure. This further leads to a slight deviation of the position parameter  $u$  from the ideal  $uc/a=(3/8)^{1/2}$  as the hexagonal packing becomes denser. The observed changes in the  $d(100)/d(002)$  ratio for the hexagonal phase and the  $d(020)/d(220)$  ratio for the cubic phase correlate highly with the pressure variations over the studied range in S1, S2, and T1 (see Figs. 5 and S5). Specifically, the ratio  $d(100)/d(002)$  increases linearly with pressure before the phase transformation and deviates from the linear relationship in the transition zone, while the ratio  $d(020)/d(220)$  decreases slightly with pressure after the phase transition. Such anisotropic compression behavior indicates that both *w*-ZnO and *rs*-ZnO phases are distorted in the transition zone, as discussed previously in ref. [47].

Observations of non-consistent transformation reversibility of the *rs*-ZnO phase have been a central issue for a long time. Various experiments showed that the transition from *rs* phase to *w* phase returns to *rs* phase with pronounced hysteresis [52,63,55], while other experiments showed that the partially extinguished *rs* phase persists with *w* phase at ambient conditions. Such a rather contradictory phenomenon [47–51,87,88] has addressed the unsolved question - why do the phase-pure ZnO samples of the cubic assemblies show different transformation activities under the same pressure ranges? Recently, it has been proposed that such delicate behavior results from surface energy differences [47,82] between the crystalline phases and the volume collapse ratio. Furthermore, particle size significantly affects the pressure range of phase stability and the final fractions of *rs* and *w* phases at ambient conditions [47] in various ZnO samples. As suggested by Liu et al. [59] a plausible explanation for such different reversibility phenomena observed in S1, S2, and T1 is that a small amount of the *rs* phase trapped in the nanoscale grain size during the *w* to *rs* transition upon compression and then the *rs* to *w* transition upon decompression, resulting in the partial visibility of the *rs* phase even after the pressure is released. Moreover, the mechanism of pressure hysteresis strongly reflects the effects of crystallite size and lattice strain [89–93]. Remarkably, Fig. 6a shows a clear trend – as the applied pressure is increased, we observed a more pronounced reduction in crystallite size. The most striking observation that emerges from the comparison of the S1, S2, and T1 data is an abrupt change in crystallite size in the sample T1, observed from 94.1(1) at 0 GPa to 62.2(1) at 0.36 GPa. In contrast, no significant difference in crystallite size values was observed in the other two ZnO samples over such a very narrow pressure range.

In order to get further insight into the role of the compression behavior of the high-pressure phases in ZnO samples, mapping of the surface morphology at ambient conditions (see Figs. S6–S8), were combined with the results of the line broadening analysis (Fig. 6). We observed that the crystallites formed in the sample T1 are larger, implying a smaller surface area [94], and thus favor a reversible transformation process from cubic to hexagonal symmetry upon decompression. As obtained from the BET surface area analysis, with an increase in crystallite size the specific surface areas decrease from 10.65(15) in sample S1 to 2.75(6) m<sup>2</sup>/g in sample T1. On the other hand, the much smaller crystallites of 45.9(1) and 18.9(1) nm in S1 and S2, respectively, promote rather striking stability of the cubic lattice and potentially hinder the transformation process upon decompression to 0 GPa. In general, the higher phase transition

pressure compared to the bulk is consistent with previous results[47] and is attributed to the large surface-to-volume ratio[95]of the nanocrystals. Independent of the contribution of the crystallite size, the phase transition process is also largely related to the transition-induced elastic strain[83] arising from the lattice differences between hexagonal and cubic phases. Based on the Rietveld refinements, the evolution of lattice microstrain as a function of applied pressure in S1,S2, and T1 did not show the same trend of change over the same pressure range, as shown in Fig. 6. Prior to the hexagonal to a cubic phase transition, the average lattice microstrain increases with pressure in an almost exponential manner in both hydrothermally produced and calcined ZnO samples. At the onset of the phase transition, the lattice strain in the sample S1 decreases steeply with pressure indicating the occurrence of plastic flow[96],which leads to a further decrease in the strength of each phase, thus showing similarities with commercially available polycrystalline ZnO powder, such as ref.[47]. The occurrence of plastic flow can relax the internal strain, allowing further growth of the cubic phase[96,97]. On the other hand, at low pressure, there is a pure hexagonal phase with large lattice strain in both samples,S2 and T1, while a discontinuity in the strain is visible during the phase transition. After the phase transition, the lattice microstrain remains relatively stable at higher pressures in all prepared samples.Undoubtedly, a larger microstrain reduces the crystallite size, strengthens the bond bending, and thus has a strong influence on the reversibility phenomena and mechanical properties of the ZnO particles[98,99].

### *3.2 Photocatalytic degradation of RhB dye*

Results from the photocatalytic activity of three ZnO samples towards the RhB pollutant, a carcinogenic textile dye are shown in the left panel of Fig. 7, where the sample S1 exhibits the highest photocatalytic activity among three. The blank test was carried out by illuminating a UV source on the RhB dye solution directly without catalyst (Fig. S9).During the adsorption process, S1 removed 14 % of the RhB dye, whereas the samples S2 and T1 removed 2 % and 4 % of pollutant molecules, respectively. In general, the RhB solution is quite stable once illuminated [38]– negligible wavelength shifts and absorption peak intensities are observed under illumination, while the addition of S1, S2, and T1 photocatalysts leads to a steep decrease in adsorption at 554 nm with irradiation time. A significant increase in photocatalytic activity towards photodegradation of RhB footprints was observed for S1 and S2 photocatalysts under UV irradiation for 50

min, while T1 showed complete degradation after 200 min treatment time. In general, the RhB solution is quite stable once illuminated [38]—negligible wavelength shifts and absorption peak intensities are observed under illumination, while the addition of S1, S2, and T1 photocatalysts leads to a steep decrease in adsorption at 554 nm with irradiation time. Based on a comparison of the regression coefficients,  $R^2$ , the photocatalytic dye degradation reaction is assumed to follow first-order kinetics (Table 2), which ensures the model Langmuir–Hinshelwood [100]. The photocatalytic RhB degradation rates using different ZnO catalysts are tabulated in Table 2. As shown in Fig. 7e, the apparent rate constants of the products increased from  $1.56(1) \times 10^{-2} \text{ min}^{-1}$  to  $9.7(2) \times 10^{-2} \text{ min}^{-1}$ , in the order  $T1 > S2 > S1$ , while  $k_{app}$  was only  $5 \times 10^{-4} \text{ min}^{-1}$  in the blank experiment.

Various efforts have been made to improve the photocatalytic activity of ZnO catalysts by modifying their surface and structure [38, 101–111], but to our knowledge no other author has found such a high first-order rate constant for a pure ZnO photocatalyst prepared by the methods we described in this study. Our results differ significantly from previous results reported in the literature, where the degradation rate of the RhB solution was improved after the addition of pure ZnO, but still showed a rather poor degradation activity, with  $k_{app}$  in the range of  $3.96 \times 10^{-3}$  to  $2.5 \times 10^{-2} \text{ min}^{-1}$  [36, 104]. The sample S1 showed the best photocatalytic activity (Fig. 7f) for RhB dye degradation in 50 min (about 99 % degradation). Degradation with S2 was also found to be as high as 98 %, while T1 showed a significantly low 53 % degradation, of which the latter is related to the decrease in the specific surface area obtained from the BET analysis. It is critical to note that the result for the S1 degradation effect over the RhB dye solution is comparable to the result reported for the plasma modified [36] ZnONPs, which efficiently degraded the RhB solution by 97.8 % in 40 min. As far as the photocatalyst stability is concerned, the photocatalytic reactions of optimal catalyst (i.e. sample S1) over RhB dye pollutant were repeated under the same reaction conditions within 3 cycles at pH=7 (see Fig. S10, Table S2). The slightly lower activity of recycled S1 in the third cycle (i.e. the degradation reduced from ~99% in the first cycle to ~96% in the third cycle) resulted in only ~3 % loss of RhB degradation.

### *3.3 Surface diversity of ZnO samples identified by XPS characterization*

Photoemission spectra around the O 1s corelevels of S1, S2, and T1 are shown in Fig. 8. All spectra show a similar structure: the main peak at the binding energy (BE) of 530.0 eV and a smaller feature shifted to a higher BE of 531.5 eV. We assign the dominant line to the O 1s emission corresponding to electrons from the Zn-O bonds ( $O^{2-}$  ions) originating from the oxygen of the ZnO crystal lattice[103,112]. On the other hand, the additional peak at 531.5 eV is attributed to oxygen or hydroxide species[113]. Indeed, the physically absorbed OH radicals ( $\cdot OH$ )[114] are an important active species in semiconductor photocatalysis. The relative fraction of the chemisorbed O or OH groups is largest in sample S1, with a relative contribution of 30 % (compared to 23 % in T1 and 21 % in S2). We explain this difference by a higher adsorption affinity for O or OH species on the S1 surface, which in turn may contribute to the enhanced photocatalytic activity observed for this sample. Indeed, the amount of O or OH species on surfaces of photocatalytic materials was previously found to play an important role in photocatalytic activity, leading to more efficient photocatalytic activity on surfaces with a higher concentration of oxygen or  $\cdot OH$ . The difference in the atomic structures of the surfaces may lead to the discrepancy in the ability of chemisorbed oxygen species or  $\cdot OH$ [115,116].

### *3.4 ZnO particles affecting the photocatalytic activity through the bandgap calculations*

The impact of morphologically tuned nano- and micro-sized ZnO particles on photocatalytic activity was elucidated through the energy bandgap calculations as the change in the value of the bandgap can be attributed to the effect of the ZnO particle size [117, 118, 119]. As can be seen from Fig. S11, the UV–Vis absorption spectra of ZnO samples are characterized by broad and intensive absorption between 200 and 400 nm. A significant increase in the absorption at wavelengths shorter than 400 nm can be assigned to the intrinsic bandgap absorption of ZnO due to the electron transitions from the valence band to the conduction band ( $O_{2p} \rightarrow Zn_{3d}$ ) [120]. The as-prepared powder had no optical absorption in the visible region, but there was a good absorption nearly in the whole UV region. The direct bandgap energies estimated from the intercept of the tangents to the plots from Fig. S11 are found to be 3.23 eV, for S1, 3.22 eV for S2, and 3.18 eV for T1. These  $E_g$  values are slightly higher compared to those reported by J. Yu and X. Yu for ZnO hollow spheres [120]. Furthermore, observation shows that spherical ZnONPs (i.e.



samples S1 and S2) feature a blue-shifted UV absorption edge with respect to the absorbance of the tubular sample T1 that was prepared in an aqueous NaOH solution. This shift is caused by the strengthening of the quantum confinement of charge carriers at a decrease in the size of ZnO NPs [121]. The bandgap of ZnO particles decreased with an increase in crystallite size, thus directly influencing the near band edge emission and supporting the enhanced photocatalytic decolorization of RhB aqueous solution using spherically shaped ZnO catalysts. Indeed, the ZnO samples with smaller crystallite sizes (i.e. samples S1 and S2) have a larger redox potential for photocatalytic decomposition of organic contaminants under UV irradiation [120]. The enhanced photocatalytic activity of samples S1 and S2 over T1 can be ascribed to higher specific surface areas and smaller crystallite sizes that favor the enhancement in redox potential.

### *3.5 Understanding the mechanism of ZnO NPs formation towards diverse high pressure behavior and enhanced photocatalytic activity*

Choice of the synthesis protocol among various processes will largely influence the microstructure and morphology of ZnO particles and their chemical and physical properties, which play a key role in controlling the catalytic performance and mechanical features towards improved functionalities and direct applications of this material. The mechanism governing the formation of ZnO particles has been deciphered by detailed theoretical simulations of ZnO interface-solvent and interface-additive interactions using quantum chemical calculations. In particular, we identified the mechanism of ZnO particle formation in the desired ZnO catalyst by integrating various synthetic chemistry and materials physics data (i.e. microstructure and surface behavior) using theoretical simulations of the ZnO surface/solvent and surface/additive interactions using  $(\text{ZnO})_{36}\text{-H}_2\text{O}$ ,  $(\text{ZnO})_{36}\text{-CH}_3\text{CH}_2\text{OH}$ ,  $(\text{ZnO})_{36}\text{-CH}_3(\text{CH}_2)_7\text{OH}$ , and  $(\text{ZnO})_{36}\text{-TEA}$  models (Fig. S12). The  $(\text{ZnO})_{36}$  cluster served as a suitable model [61] for cluster modeling. The most stable  $(\text{ZnO})_{36}\text{-H}_2\text{O}$ -,  $(\text{ZnO})_{36}\text{-CH}_3\text{CH}_2\text{OH}$ -,  $(\text{ZnO})_{36}\text{-CH}_3(\text{CH}_2)_7\text{OH}$ - and  $(\text{ZnO})_{36}\text{-TEA}$ -structures, as well as the bond lengths (d), energies (E), and QTAIM properties of the selected bonds, are summarized in Table S3. The calculated values of the Gibbs free energies of the surface/additive interaction are given in Table S3, while the total electronic energies, thermal corrections to the Gibbs

free energy, total free energies of the resulting and associating unit structures are given in Table S4. The primary ZnO NPs in sample S2 showed a high tendency to spherical aggregation, while no significant tendency to spherical aggregation of fine uniform NPs was observed in the ethanol media. Most likely, such treatment enables a sufficient combination of favorable electrostatic interaction between ZnO NPs, small polar molecules of ethanol, and the smaller amount of TEA molecules, to prevent the aggregation process. However, the aggregation of fine primary ZnO NPs into larger densely packed spheres in ethanol media is favored by increasing the TEA concentration, indicating the shaping role of TEA chains in stimulating the aggregation process [43,122]. Because of the ability of ethanolamines to combine the properties of amines and alcohols and to participate in reactions common to both groups, resulting in a considerable change in particle surface properties, good control of morphology and crystallite size is achieved by changing the nature of the alcoholic solvents and the molar ratio  $[\text{TEA}]/[\text{Zn}(\text{acac})_2]$ . Consequently, it appears that a small amount of TEA suppresses both the growth of the primary NPs and their assembly (sample S1), while the excess amount of TEA suppresses the growth of the primary NPs and mimics a bridge between adjacent ZnO NPs to form the large, spherical ZnO agglomerates (sample S2). The influence of the TEA additive on the overall shape of the ZnO NPs and their aggregates in both samples, S1 and S2, was confirmed by theoretical simulations of the surface/additive interactions using an appropriate  $(\text{ZnO})_{36}$ -TEA model.

The calculated values of Gibbs free energies showed that the  $(\text{ZnO})_{36}$ -TEA interaction is a spontaneous exergonic process in both  $\text{CH}_3\text{CH}_2\text{OH}$  and  $\text{CH}_3(\text{CH}_2)_7\text{OH}$  solvents, with Gibbs energy values of  $\Delta G^*_{\text{INT}} = -8.52 \text{ kcal mol}^{-1}$  and  $\Delta G^*_{\text{INT}} = -7.68 \text{ kcal mol}^{-1}$ , respectively (see Table S2). However, the possible surface/solvent  $(\text{ZnO})_{36}$ - $\text{CH}_3\text{CH}_2\text{OH}$  or  $(\text{ZnO})_{36}$ - $\text{CH}_3(\text{CH}_2)_7\text{OH}$  interactions imply the structures for which the interactions are slightly endergonic processes ( $\Delta G^* > 0$ ). Due to the high chelating efficiency of TEA over Zn, a structural motif was observed in the  $(\text{ZnO})_{36}$ -TEA model, where TEA appears to be anchored to the  $(\text{ZnO})_{36}$  cluster by three extremely strong hydrogen  $\text{O}-\text{H}\cdots\text{O}$  bonds, which are accomplished between the hydrogen atom of TEA hydroxyl groups and the oxygen in the  $(\text{ZnO})_{36}$  cluster, increasing its stability (Fig. 9).

It is important to emphasize that the growth control of the primary ZnO NPs is ensured by the prevention of the growth of the cores and the bare ZnO NPs in the first phase due to the good adsorption of three flexible hydroxyl chains of the TEA molecules on their surfaces. Indeed, the calculated values of the binding energies indicate the unusual strength of the O—H···O-hydrogen bonds between the hydrogen atom of the TEA - hydroxyl groups with the oxygen in the (ZnO)<sub>36</sub> cluster, which turned out to be the most important parameter, since the control of the surface/additive interactions allows the nuclei and the bare ZnO ultrasmall NPs to grow not only along the preferred axis. As described in the literature review[101,112,124], joint experimental and theoretical studies showed a strong dependence of the photocatalytic performance on the crystal facet exposures in the order {0001} > {10 $\bar{1}$ 1} > {10 $\bar{1}$ 0}, with the polar {0001} being the predominant facet of the spherical ZnONPs. The presence of a significant amount of TEA increases the number of TEA anchor sites resulting in higher coverage of the ZnO surface, which in turn results in higher photocatalytic efficiency of the NPs.

The calculated values of hydrogen bonding energies obtained from the surface/additive interactions in the (ZnO)<sub>36</sub>—TEA model showed that the use of ethanol as a solvent is likely to lead to much stronger bonding in the sample S1 (i.e.  $E_{O\cdots H}$  ranges from -39.76 kcal mol<sup>-1</sup> to -40.61 kcal mol<sup>-1</sup>), and weaker in sample S2 (i.e.  $E_{O\cdots H}$  ranges from -28.79 kcal mol<sup>-1</sup> to -31.67 kcal mol<sup>-1</sup>). Moreover, the aggregation process of the spherical ZnO agglomerates is mainly driven by the use of various interactions of alcoholic solvents and TEA molecules and their intermediate species with the surface of the primary ZnO NPs. Due to the high affinity of TEA and alcohol molecules for the (ZnO)<sub>36</sub> surface, based on the simultaneous involvement of both, a high degree of coverage is achieved and the particle size is limited on one side. On the other hand, all the free hydroxyl groups have a large capacity to attract each other through hydrogen bonding and serve as a link between the neighboring ZnO NPs. In addition, it is important to emphasize the influence of the weaker N—H···O-hydrogen bonds between the nitrogen atom of the amine group TEA and the oxygen in the (ZnO)<sub>36</sub> cluster on the process of spherical aggregation. In contrast, in the aqueous NaOH solution (i.e. preparation of the sample T1), hierarchical crystal growth is present along the *c*-axis by aggregation of hollow tubular ZnO substructures with lamellar hexagonal stacking. The growth process of the hollow spindle-shaped

particles is complex and has been proposed based on a combined experimental and theoretical approach. The main driving forces responsible for the preferential orientation growth along the *c*-axis of the hollow spindle-shaped particles, which is favored in the aqueous NaOH solution, are various interactions of the water-solvent molecules, as well as hydroxyl groups from NaOH, with the surface of ZnO. Interestingly, the transfer of a hydrogen atom from the water molecule to oxygen in the (ZnO)<sub>36</sub> cluster is observed in the most stable (ZnO)<sub>36</sub>–H<sub>2</sub>O structure (Table S1). As a result of this process, a free pair of electrons on the oxygen atom of the water molecule participated in a new strong coordinate bond with zinc (Zn–O):  $d_{\text{Zn-O}} = 2.029 \text{ \AA}$ ,  $E_{\text{Zn-O}} = -29.15 \text{ kcal mol}^{-1}$ . According to the topological parameters  $H(r_c) < 0$  and  $\nabla^2\rho(r_c) > 0$  summarized in Table S3, the Zn–O bond was assigned to an intermediate interaction type, which is a feature of coordinate bonding. Due to the high affinity of the H<sub>2</sub>O molecules for the (ZnO)<sub>36</sub> surface, which is based on the simultaneous bonding by the transfer of hydrogen atoms and the Zn–O bond, high free energy is released ( $\Delta G^*_{\text{INT}} = -6.74 \text{ kcal mol}^{-1}$ ). It seems that the spontaneous deprotonation of H<sub>2</sub>O molecules, observed in the most stable (ZnO)<sub>36</sub>–H<sub>2</sub>O structure (Table S3), as well as the presence of NaOH where the surface of ZnO NPs is directly attacked with OH ions, play a key role in explaining the hierarchical crystal growth along the *c*-axis through the aggregation of hollow tubular ZnO substructures[124] with lamellar hexagonal stacking. The Cartesian coordinates of the calculated clusters are given in the Supplementary Information (see Tables S6 to S10).

#### 4. Conclusions

This paper underlines the importance of theoretical understanding beyond systematic pathway set-ups, which can lead to the designing of morphologically targeted ZnO NPs. By integrating synthesis of ZnO particles using three different methods, and structural/chemical property measurements, aided by theory calculations we singled out the optimal ZnO candidate with morphology-dependent functionalities.

We studied the microstrain responses of the shape-selected ZnO NPs to the applied hydrostatic pressure up to 30 GPa and carried out degradation measurements over the RhB dye pollutant molecules. This comparative study revealed that the diversity of size and shape of ZnO particles distinguishes the *w-to-rs* transformation reversibility

phenomena by dictating the microstructure-dependent deformation behavior and ultimately leading to different microstrain responses to hydrostatic pressure. We have highlighted the exceptionally high apparent-rate constant of  $9.7(2)\times 10^{-2} \text{ min}^{-1}$ , which relegates the role of spherical ZnO NPs grown hydrothermally from ethanolic solution towards the giant, spindle-shaped ZnO particles prepared in NaOH medium with calcination treatment.

It seems that by understanding the crystal growth of ZnO NPs *via* the molecular ZnO interface/solvent/additive interactions and screening the solution chemistry of ZnO NPs, one can make ZnO a highly efficient promising multifunctional material. The prospect of being able to synthesize pure ZnO NPs that efficiently degrade ~99 % of the RhB dye pollutant in 50 min serves as a continuous incentive for future research. Preliminary studies showed that spherically shaped ZnO catalyst prepared from ethanolic solution can be conveniently recovered and reused for three runs with a 3 % loss of RhB degradation. Our results are encouraging and should be validated by a larger series of samples and probing different factors affecting the photocatalytic degradation of pollutant molecules.

### **Supplementary information**

Supplementary information accompanies this paper.

### **Authors' contributions**

M.V. conceived the project, designed experiments, and contributed to conceptualization; M.V., Y.D., and D.L.H. are responsible for raising funds; A.Š. developed and optimized the synthesis method, and contributed to DFT integration in predicting the mechanism of ZnO formation; M.V. performed SPXRD characterization work; T.N. performed the high-pressure SPXRD measurements and contributed to the SPXRD analysis; H.I. and N.H. contributed to the high-pressure SPXRD experiments; I.D. performed the computational work; L.K. performed and interpreted the photocatalytic activity measurements; G.D. performed the TEM measurements; R.P. and M.P. performed and analyzed the XPS measurements. All authors contributed to the paper, which was written by M.V.

## **Declaration of Competing Interest**

The authors declare that they have no known competing financial interests or personal relationships that could have appeared to influence the work reported in this paper.

## **Acknowledgments**

We thank SPring-8 for providing the synchrotron radiation facilities and we thank H.I. and N.H. for assistance in the use of the beamline. M.V. gratefully acknowledges financial support from the Croatian Academy of Sciences. M.V. gratefully acknowledges the support of the project co-funded by the Croatian Government and the European Union through the European Regional Development Fund – Competitiveness and Cohesion Operational Programme (Grant KK.01.1.1.01.0001). M.V. and Y.D. gratefully acknowledge support from the bilateral project Croatian–Chinese in 2019–2021. M.V. and D.L.H. gratefully acknowledge support from the bilateral project Croatian–German(DAAD) in 2019–2021. G.D. gratefully acknowledges financial support from the Slovenian Research Agency (P2–0393).The experiments on the Taiwanese BL12B2 sector of SPring-8 were carried out under Proposal No.2018B4141 and No.2019A4132.R.P. and M. P. gratefully acknowledge support from the University of Rijeka under Project No. 18-144. The authors thank Zagreb University Computing Centre (SRCE) for generously granting computing resources on the cluster ISABELLA.

## **Supplementary materials**

Supplementary material associated with this article can be found, in the online version.

## **References**

- 1 L. Wang, M. Muhammed, Synthesis of zinc oxide nanoparticles with controlled morphology, *J. Mater. Chem.* 9 (1999) 2871–2878.
- 2 P. Sivakumar, M. Lee, Y.-S. Kim, M.S. Shim, Photo-triggered antibacterial and anticancer activities of zinc oxide nanoparticles, *J. Mater. Chem. B* 6 (2018) 4852–4871.
- 3 P. Banerjee, P.K. Jain, Mechanism of sulfidation of small zinc oxide nanoparticles *RSC Adv.* 8 (2018) 34476–34482.

- 4 D.G. Georgiadou, J. Semple, A.A. Sagade, H. Forstén, P. Rantakari, Y.-H. Lin, F. Alkhalil, A. Seitkhan, K. Loganathan, H. Faber, T.D. Anthopoulos, 100 GHz zinc oxide Schottky diodes processed from solution on a wafer scale, *Nat. Electron.* 3(2020) 718–725.
- 5 A. Narayana, S.A. Bhat, A. Fathima, S.V. Lokesh, S.G. Suryad, C.V. Yelamaggad, Green and low-cost synthesis of zinc oxide nanoparticles and their application in transistor-based carbon monoxide sensing, *RSC Adv.* 10(2020) 13532–13542.
- 6 P. Amuthavalli, J.-S. Hwang, H.-U. Dahms, L. Wang, J. Anitha, M. Vasanthakumaran, A.D. Gandhi, K. Murugan, J. Subramaniam, M. Paulpandi, B. Chandramohan, S. Singh, 2021. Zinc oxide nanoparticles using plant *Lawsonia inermis* and their mosquitocidal, antimicrobial, anticancer applications showing moderate side effects. *Sci. Rep.* 11, 8837.
- 7 Z.L. Wang, Splendid one-dimensional nanostructures of zinc oxide: a new nanomaterial family for nanotechnology, *ACS Nano* 2 (2008) 1987–1992.
- 8 P. Yang, R. Yan, M. Fardy, Semiconductor nanowire: what's next? *Nano Lett.* 10 (2010) 1529–1536.
- 9 U. Ozgur, Y.I. Alivov, C. Liu, A. Teke, M.A. Reshchikov, S. Doğan, V. Avrutin, S.-J. Cho, H. Morkoç, 2005. A comprehensive review of ZnO materials and devices *J. Appl. Phys.* 98, 041301.
- 10 J. Zhou, N.S. Xu, Z.L. Wang, Dissolving behavior and stability of ZnO wires in biofluids: a study on biodegradability and biocompatibility of ZnO nanostructures, *Adv Mater.* 18(2006)2432–2435.
- 11 A. Kołodziejczak-Radzimska, T. Jesionowski, Zinc Oxide—From Synthesis to Application: A Review, *Materials*, 7 (2014) 2833–2881.
- 12 B. Zhang, F. Wang, C. Zhu, Q. Li, J. Song, M. Zheng, L. Ma, W. Shen, A Facile Self-assembly Synthesis of Hexagonal ZnO Nanosheet Films and Their Photoelectrochemical Properties, *Nano-Micro Lett.* 8(2016) 137–142.
- 13 R. Shwetharani, H.R. Chandan, M. Sakar, G.R. Balakrishna, K.R. Reddy, A.V. Raghu, Photocatalytic semiconductor thin films for hydrogen production and environmental applications, *Int. J. Hydrogen Energy*, 45 (2020) 18289–18308.

- 14 H. Wang, P. Zhang, Z. Zang, 2020. High performance CsPbBr<sub>3</sub> quantum dots photodetectors by using zinc oxide nanorods arrays as an electron-transport layer, *Appl. Phys. Lett.*, 116, 162103.
- 15 H. Wang, S. Cao, B. Yang, H. Li, M. Wang, X. Hu, K. Sun, Z. Zang, 2019. NH<sub>4</sub>Cl-Modified ZnO for High-Performance CsPbI<sub>2</sub>Br<sub>2</sub> Perovskite Solar Cells via Low Temperature Process, *Sol. RRL*, 1900363.
- 16 Z. Zang, 2018. Efficiency enhancement of ZnO/Cu<sub>2</sub>O solar cells with well oriented and micrometer grain sized Cu<sub>2</sub>O films, *Appl. Phys. Lett.*, 112, 042106.
- 17 S. Cao, H. Wang, H. Li, J. Chen, Z. Zang, 2020. Critical role of interface contact modulation in realizing low-temperature fabrication of efficient and stable CsPbI<sub>2</sub>Br<sub>2</sub> perovskite solar cells, *Chem. Eng. J.*, 394, 124903.
- 18 J. Li, J. Xia, Y. Liu, S. Zhang, C. Teng, X. Zhang, B. Liu, S. Zhao, S. Zhao, B. Li, G. Xing, F. Kang, G. We, 2020. Ultrasensitive Organic-Modulated CsPbBr<sub>3</sub> Quantum Dot Photodetectors via Fast Interfacial Charge Transfer, *Adv. Mater. Interfaces*, 7, 1901741.
- 19 Z.L. Wang, Nanostructures of zinc oxide, *Mater. Today* 7 (2020) 26–33.
- 20 K. Kannana, D. Radhika, K.K. Sadasivunia, K.R. Reddy, A.V. Raghu, 2020. Nanostructured metal oxides and its hybrids for biomedical applications, *Adv. Colloid Interface Sci.*, 281, 102178.
- 21 N. Wiesmann, W. Tremel, J. Briegera, Zinc oxide nanoparticles for therapeutic purposes in cancer medicine, *J. Mater. Chem. B* 8 (2020) 4973–4989.
- 22 M. Hamdi, H.M. Abdel-Bar, E. Elmowafy, A. El-khouly, M. Mansour, G.A.S. Awad, Investigating the Internalization and COVID-19 Antiviral Computational Analysis of Optimized Nanoscale Zinc Oxide, *ACS Omega* 6 (2021) 6848–6860.
- 23 G.H. Attia, Y.S. Moemen, M. Youns, A.M. Ibrahim, R. Abdou, M.A. El Raeyh, 2021. Antiviral zinc oxide nanoparticles mediated by hesperidin and in silico comparison study between antiviral phenolics as anti-SARS-CoV-2, *Colloids Surf. B Biointerfaces*. 203, 111724.
- 24 K. Kannan, D. Radhika, K.R. Reddy, A.V. Raghu, K.K. Sadasivuni, G. Palani, K. Gurushankar, 2020. Gd<sup>3+</sup> and Y<sup>3+</sup> co-doped mixed metal oxide nanohybrids for photocatalytic and antibacterial applications, *Nano Ex.*, 2, 010014.



- 25 K. Kannan, D. Radhika, A.S. Nesaraj, K.K. Sadasivuni, K.R. Reddy, D. Kasai, A.V. Raghu, Photocatalytic, antibacterial and electrochemical properties of novel rare earth metal oxides-based nanohybrids, *Mater. Sci. Energy. Technol.* 3 (2020) 853–861.
- 26 M. Srinivas, R.C. Venkata, R.R. Kakarla, N.P. Shetti, M.S. Reddy, A.V. Raghu, 2019. Novel Co and Ni metal nanostructures as efficient photocatalysts for photodegradation of organic dyes, *Mater. Res. Express*, 6, 125502.
- 27 Q. Tian, W. Yao, W. Wu, C. Jiang, NIR light-activated upconversion semiconductor photocatalysts. *Nanoscale Horiz.* 4 (2019) 10–25.
- 28 C. Byrne, G. Subramanian, S.C. Pillai, Recent advances in photocatalysis for environmental applications *J. Environ. Chem. Eng.* 6 (2018) 3531–3555.
- 29 T. Sh. Atabev, A. Molkenova, Upconversion optical nanomaterials applied for photocatalysis and photovoltaics: Recent advances and perspectives, *Front. Mater. Sci.* 13 (2019) 335–341.
- 30 X. Zhang, Y.L. Chen, R.S. Liu, D.P. Tsai, 2013. Plasmonic photocatalysis. *Rep. Prog. Phys.*, 76, 046401.
- 31 M.E. Khan, A. Mohammad, M.H. Cho (2020) Nanoparticles based Surface Plasmon Enhanced Photocatalysis. In: Naushad M., Rajendran S., Lichtfouse E. (eds) *Green Photocatalysts. Environmental Chemistry for a Sustainable World*, vol 34. Springer, Cham. pp 133-143.
- 32 F. Pincella, K. Isozaki, K.A. Miki, 2014. A visible light-driven plasmonic photocatalyst. *Light Sci. Appl.*, 3, e133.
- 33 T. Bora, D. Zoepfl, J. Dutta, 2016. Importance of Plasmonic Heating on Visible Light Driven Photocatalysis of Gold Nanoparticle Decorated Zinc Oxide Nanorods. *Sci. Rep.* 6, 26913.
- 34 R. Saravanan, S. Karthikeyan, V.K. Gupta, G. Sekaran, V. Narayanan, A. Stephen, Enhanced photocatalytic activity of ZnO/CuO nanocomposite for the degradation of textile dye on visible light illumination, *Mater. Sci. Eng. C33* (2013) 91–98.
- 35 S. Kant, D. Pathania, P. Singh, P. Dhiman, A. Kumar, Removal of malachite green and methylene blue by  $\text{Fe}_{0.01}\text{Ni}_{0.01}\text{Zn}_{0.98}\text{O}$ /polyacrylamide nanocomposite using coupled adsorption and photocatalysis, *Appl. Catal. B* 147 (2014) 340–352.

- 36 M. Pirhashemi, A. Habibi-Yangjeh, Novel ZnO/Ag<sub>2</sub>CrO<sub>4</sub> nanocomposites with n–n heterojunctions as excellent photocatalysts for degradation of different pollutants under visible light, *J. Mater. Sci.: Mater. Electron.* 27 (2016) 4098–4108.
- 37 D. Neena, K.K. Kondamareddy, H. Bin, D. Lu, P. Kumar, R.K. Dwivedi, V.O. Pelenovich, X.-Z. Zhao, W. Gao, D. Fu, 2018. Enhanced visible light photodegradation activity of RhB/MB from aqueous solution using nanosized novel Fe-Cd co-modified ZnO, *Sci. Rep.* 8, 10691.
- 38 S. Ma, Y. Huang, R. Hong, X. Lu, J. Li, Y. Zheng, 2021. Enhancing Photocatalytic Activity of ZnO Nanoparticles in a Circulating Fluidized Bed with Plasma Jet, *Catalysts.* 11, 77.
- 39 D. Liu, W. Wu, Y. Qiu, S. Yang, S. Xiao, Q.-Q. Wang, L. Ding, J. Wang, Surface Functionalization of ZnO Nanotetrapods with Photoactive and Electroactive Organic Monolayers, *Langmuir* 24 (2008) 5052–5059.
- 40 F. Gao, S. Aminane, S. Bai, A.V. Teplyakov, Chemical Protection of Material Morphology: Robust and Gentle Gas-Phase Surface Functionalization of ZnO with Propiolic Acid *Chem. Mater.* 29 (2017) 4063–4071.
- 41 T.B. Rawal, A. Ozcan, S.-H. Liu, S.V. Pingali, O. Akbilgic, L. Tetard, H. O'Neill, S. Santra, L. Petridis, Interaction of Zinc Oxide Nanoparticles with Water: Implications for Catalytic Activity, *ACS Appl. Nano Mater.* 2 (2019) 4257–4266.
- 42 S. Musić, A. Šarić, Formation of hollow ZnO particles by simple hydrolysis of zinc acetylacetonate, *Ceram. Int.* 38 (2012) 6047–6052.
- 43 A. Šarić, G. Štefanić, G. Dražić, M. Gotić, Solvothermal synthesis of zinc oxide microspheres, *J. Alloys Compd.* 652 (2015) 91–99.
- 44 A. Šarić, I. Despotović, G. Štefanić, G. Dražić, The Influence of Ethanolamines on the Solvothermal Synthesis of Zinc Oxide: A Combined Experimental and Theoretical Study, *ChemistrySelect* 2 (2017) 10038–10049.
- 45 A. Šarić, I. Despotović, G. Štefanić, Solvothermal synthesis of zinc oxide nanoparticles: A combined experimental and theoretical study, *J. Mol. Struct.* 1178 (2019) 251–260.
- 46 A. Šarić, I. Despotović, G. Štefanić, Alcoholic Solvent Influence on ZnO Synthesis: A Joint Experimental and Theoretical Study, *J. Phys. Chem. C* 123 (2019) 29394–29407.

- 47 J.Z. Jiang, J.S. Olsen, L. Gerward, D. Frost, D. Rubie, J. Peyronneau, Structural stability in nanocrystalline ZnO, *Europhys. Lett.* 50 (2000) 48–53.
- 48 L. Wang, H. Liu, J. Qian, Yang, Y. Zhao, Structural Stability and Compressibility Study for ZnO Nanobelts under High Pressure, *J. Phys. Chem. C* 116(2012) 2074–2079.
- 49 Z. Dong, K.K. Zhuravlev, S.A. Morin, L. Li, S. Jin, Y. Song, Pressure-Induced Structural Transformations of ZnO Nanowires Probed by X-ray Diffraction, *J. Phys. Chem. C* 116 (2012) 2102–2107.
- 50 X. Dong, F. Liu, Y. Xie, W. Shi, X. Ye, J.Z. Jiang, Pressure induced structural transition of ZnO nanocrystals studied with molecular dynamics, *Comput. Mater. Sci.* 65 (2012) 450–455.
- 51 D. Nie, T. Xue, Y. Zhang, X. Li, Synthesis and structure analysis of aluminum doped zinc oxide powders, *Sci. China Ser. B: Chem.* 51 (2008) 823–828.
- 52 S. Cui, W. Feng, H. Hu, Z. Feng, Y. Wang, Structural and electronic properties of ZnO under high pressure, *J. Alloys Compd.* 476 (2009) 306–310.
- 53 H. Bates, W.B. White, R. Roy, 1962. New High-Pressure Polymorph of Zinc Oxide, *Science* 137, 3534.
- 54 J.C. Jamieson, The phase behavior of simple compounds, *Phys. Earth Planet. Inter.* 3 (1970) 201–203.
- 55 J.M. Recio, M.A. Blanco, V. Luana, R. Pandey, L. Gerwar, J.S. Olsen, Compressibility of the high-pressure rocksalt phase of ZnO, *Phys. Rev. B* 58 (1998) 8949.
- 56 L. Gerward, J.S. Olsen, The High-Pressure Phase of Zincite, *J. Synchrotron Rad.* 2 (1995) 233–235.
- 57 H. Karzel, W. Potzel, M. Köfferlein, W. Schiessl, M. Steiner, U. Hiller, G.M. Kalvius, D.W. Mitchell, T.P. Das, P. Blaha, K. Schwarz, M.P. Pasternak, Lattice dynamics and hyperfine interactions in ZnO and ZnSe at high external pressures, *Phys. Rev. B* 53 (1996) 11425–11438.
- 58 S. Desgreniers, High-density phases of ZnO: Structural and compressive parameters, *Phys. Rev. B* 58 (1998) 14102–14105.

- 59 H. Liu, Y. Ding, M. Somayazulu, J. Qian, J. Shu, D. Häusermann, H. Mao, 2005. Rietveld refinement study of the pressure dependence of the internal structural parameter  $u$  in the wurtzite phase of ZnO, *Phys. Rev. B.* 71, 212103.
- 60 Q. Wang, S. Li, Q. He, W. Zhu, D. He, F. Peng, L. Lei, L. Zhang, Q. Zhang, L. Tan, X. Li, X. Li, Reciprocating Compression of ZnO Probed by X-ray Diffraction: The Size Effect on Structural Properties under High Pressure, *Inorg. Chem.* 57 (2018) 5380–5388.
- 61 H.K. Mao, J. Xu, P.M. Bell, Calibration of the ruby pressure gauge to 800 kbar under quasi-hydrostatic conditions, *J. Geophys. Res.* 91 (1986) 4673–4676.
- 62 A.P. Hammersley, S.O. Svensson, M. Hanfland, A.N. Fitch, D. Häusermann, Two-dimensional detector software: From real detector to idealised image or two-theta scan, *High Pres. Res.* 14(1996) 235–248.
- 63 H.M. Rietveld, A profile refinement method for nuclear and magnetic structures, *J. Appl. Crystallogr.* 2 (1969) 65–71.
- 64 X'Pert HighScore Plus Program, ver. 4.1; PANalytical B. V.: Almelo, Netherlands, 2014.
- 65 H. Toby, R. B. Von Dreele, GSAS-II: the genesis of a modern open-source all purpose crystallography software package, *J. Appl. Cryst.* 46 (2013) 544–549.
- 66 R.J. Hill, C.J. Howard, Quantitative Phase Analysis from Powder Diffraction Data using the Rietveld Method, *J. Appl. Cryst.* 20(1987) 467–474.
- 67 R.J. Angel, High-Temperature and High-Pressure Crystal Chemistry, in R.M. Hazen, R.T. Downs (Eds.), *Reviews in Mineralogy and Geochemistry*, Mineralogical Society of America & Geochemical Society, 2000, pp. 35.
- 68 J. Gonzalez-Platas, M. Alvaro, F. Nestola, R.J. Angel, EosFit7-GUI: a new graphical user interface for equation of state calculations, analyses and teaching, *J. Appl. Cryst.* 49 (2016) 1377–1382.
- 69 U.I. Gaya, *Heterogeneous Photocatalysis Using Inorganic Semiconductor Solids*, Springer, Dordrecht, 2014.
- 70 P. Sangpour, F. Hashemi, A.Z. Moshfegh, Photoenhanced Degradation of Methylene Blue on Cosputtered M:TiO<sub>2</sub> (M = Au, Ag, Cu) Nanocomposite Systems: A Comparative Study, *J. Phys. Chem. C* 114 (2010) 13955–13961.
- 71 R. Hesse, T. Chasse, R. Szargan, Peak shape analysis of core level photoelectron spectra using UNIFIT for WINDOWS, *Fresenius. J. Anal. Chem.* 365 (1999) 48–54.

- 72 J. Tauc, R. Grigorovici, A. Vancu, Optical Properties And Electronic Structure of Amorphous Germanium. *Phys. Status Solidi B*, 15 (1996) 627–637.
- 73 M.J. Frisch, G.W. Trucks, H.B. Schlegel, G.E. Scuseria, M.A. Robb, J.R. Cheeseman, G. Scalmani, V. Barone, B. Mennucci, G.A. Petersson, H. Nakatsuji, M. Caricato, X. Li, H.P. Hratchian, A.F. Izmaylov, J. Bloino, G. Zheng, J.L. Sonnenberg, M. Hada, M. Ehara, K. Toyota, R. Fukuda, J. Hasegawa, M. Ishida, T. Nakajima, Y. Honda, O. Kitao, H. Nakai, T. Vreven, J.A. Montgomery, Jr, J.E. Peralta, F. Ogliaro, M. Bearpark, J.J. Heyd, E. Brothers, K. N. Kudin, V.N. Taroverov, R. Kobayashi, J. Normand, K. Raghavachari, A. Rendell, J.C. Burant, S.S. Iyengar, J. Tomasi, M. Cossi, N. Rega, J.M. Millam, M. Klene, J.E. Knox, J.B. Cross, V. Bakken, C. Adamo, J. Jaramillo, R. Gomperts, R.E. Stratmann, O. Yazyev, A.J. Austin, R. Cammi, C. Pomelli, J.W. Ochterski, R.L. Martin, K. Morokuma, V.G. Zakrzewski, G.A. Voth, P. Salvador, J.J. Dannenberg, S. Dapprich, A.D. Daniels, Ö. Farkas, J.B. Foresman, J.V. Ortiz, J. Cioslowski, D.J. Fox, Gaussian 09, Revision D.01, Gaussian, Inc., Wallingford CT, 2009.
- 74 M. Chen, T.P. Straatsma, Z. Fang, D.A. Dixon, Structural and Electronic Property Study of (ZnO)<sub>n</sub>, n ≤ 168: Transition from Zinc Oxide Molecular Clusters to Ultrasmall Nanoparticles, *J. Phys. Chem. C* 120 (2016) 20400–20418.
- 75 A.V. Marenich, C.J. Cramer, D.G. Truhlar, Universal Solvation Model Based on Solute Electron Density and on a Continuum Model of the Solvent Defined by the Bulk Dielectric Constant and Atomic Surface Tensions, *J. Phys. Chem. B* 113 (2009) 6378–6396.
- 76 Y. Zhao, N.E. Schultz, D.G. Truhlar, Design of Density Functionals by Combining the Method of Constraint Satisfaction with Parametrization for Thermochemistry, Thermochemical Kinetics, and Noncovalent Interactions, *J. Chem. Theory Comput.* 2 (2006) 364–382.
- 77 P.J. Hay, W.R. Wadt, Ab initio effective core potentials for molecular calculations. Potentials for the transition metal atoms Sc to Hg, *J. Chem. Phys.* 82 (1985) 270–283.
- 78 R.F.W. Bader, *Atoms in Molecules: a Quantum Theory*, Clarendon Press, Oxford, 1990.
- 79 T.A. Keith, AIMAll (Version 17.01.25). TK Gristmill Software, Overland Park KS, USA, 2017.

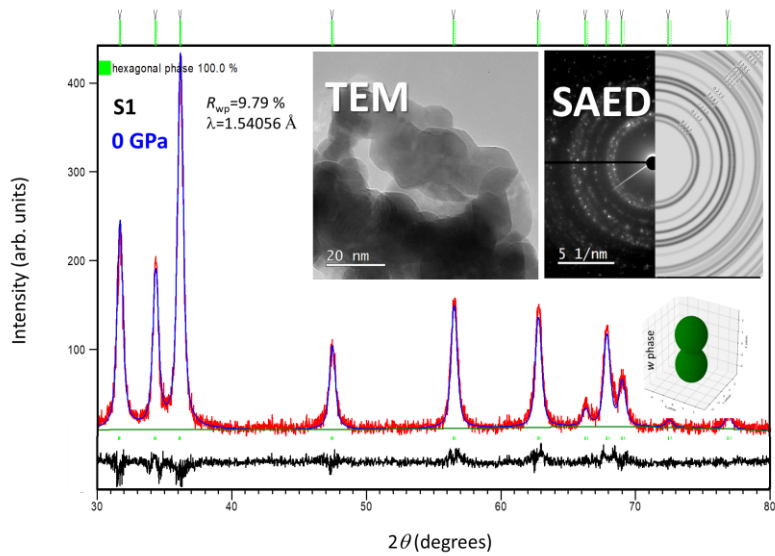
- 80 F. Decremps, F. Datchi, A.M. Saitta, A. Polian, S. Pascarelli, A. Di Cicco, J.P. Itié, F. Baudelet, 2003. Local structure of condensed zinc oxide, *Phys. Rev. B*. 68, 104101.
- 81 G.J. Hanna, S.T. Teklemichael, M.D. McCluskey, L. Bergman, J. Huso, 2011. Equations of state for ZnO and MgZnO by high pressure x-ray diffraction, *J. Appl. Phys.* 110, 073511.
- 82 X. Wu, Z. Wu, Lin Guo, C. Liu, J. Liu, X. Li, H. Xu, Pressure-induced phase transformation in controlled shape ZnO nanorods, *Solid State Commun.* 135 (2005) 780–784.
- 83 X. Yan, H. Dong, Y. Li, C. Lin, C. Park, D. He, W. Yang, 2016. Phase transition induced strain in ZnO under high pressure, *Sci. Rep.* 6, 24958.
- 84 S. Limpijumnong, W.R. Lambrecht, Homogeneous strain deformation path for the wurtzite to rocksalt high-pressure phase transition in GaN, *Phys. Rev. Lett.* 86 (2001) 91–94.
- 85 K. Inoue, Ph. D. Thesis, University of Tokyo, Tokyo, 1975, 89.
- 86 C. Kittel, *Introduction to Solid State Physics*, eighth ed., John Wiley & Sons, 2004.
- 87 L. Liu, *High-Pressure Research: Applications in Geophysics*, Academic Press, New York, 1977, 245.
- 88 E. Ito, Y. Matsui, High-pressure synthesis of ZnSiO<sub>3</sub> ilmenite, *Phys. Earth Planet. Inter.* 9 (1974) 344–352.
- 89 S.H. Tolbert, A.P. Alivisatos, Size dependence of a first order solid-solid phase transition: the wurtzite to rock salt transformation in CdSe nanocrystals, *Science* 265 (1994) 373.
- 90 S.H. Tolbert, A.P. Alivisatos, The wurtzite to rock salt structural transformation in CdSe nanocrystals under high pressure, *J. Chem. Phys.* 102 (1995) 4642–4656.
- 91 S.H. Tolbert, A.B. Herhold, L.E. Brus, A.P. Alivisatos, Pressure-induced structural transformations in Si nanocrystals: surface and shape effects, *Phys. Rev. Lett.* 76 (1996) 4384–4387.
- 92 S.B. Qadri, J. Yang, B.R. Ratna, E.F. Skelton, J.Z. Hu, Pressure induced structural transitions in nanometer size particles of PbS, *Appl. Phys. Lett.* 69 (1996) 2205–2207.

- 93 J.Z. Jiang, L. Gerward, D. Frost, R. Secco, J. Peyronneau, J.S. Olsen, Grain-size effect on pressure-induced semiconductor-to-metal transition in ZnS, *J. Appl. Phys.* 86 (1999) 6608–6610.
- 94 Y.F. Chen, C.Y. Lee, M.Y. Yeng, H.T. Chiu, The effect of calcination temperature on the crystallinity of TiO<sub>2</sub> nanopowders, *J. Cryst. Growth* 247 (2003) 363–370.
- 95 A.P. Alivisatos, Perspectives on the Physical Chemistry of Semiconductor Nanocrystals, *J. Phys. Chem.* 100 (1996) 13226–13239.
- 96 H. Marquardt, L. Miyagi, Slab stagnation in the shallow lower mantle linked to an increase in mantle viscosity, *Nat. Geosci.* 8 (2015) 311–314.
- 97 T. Kubo, E. Ohtani, T. Kato, T. Shinmei, K. Fujino, Effects of Water on the  $\alpha$ - $\beta$  Transformation Kinetics in San Carlos Olivine, *Science* 281 (1998) 85–87.
- 98 J.L. Mosenfelder, J.A.D. Connolly, D.C. Rubie, M. Liu, Strength of (Mg,Fe)<sub>2</sub>SiO<sub>4</sub> wadsleyite determined by relaxation of transformation stress, *Phys. Earth Planet. Inter.* 120 (2000) 63–78.
- 99 Y. Ma, Y.C. Chang, J.Z. Yin, Evaluation of lattice strain in ZnO thin films based on Williamson-Hall analysis, *J. Optoelectron. Adv. M.* 21 (2019) 702–709.
- 100 R. Ghosh, D. Basak, S. Fujihara, Effect of substrate-induced strain on the structural, electrical, and optical properties of polycrystalline thin films, *J. Appl. Phys.* 96 (2004) 2689–2692.
- 101 K.J. Laidler, J.H. Meiser, *Physical Chemistry*, Benjamin/Cummings, 1982, p.780.
- 102 S. Cho, S.-H. Jung, K.-H. Lee, Morphology-controlled growth of ZnO nanostructures using microwave irradiation: From basic to complex structures, *J. Phys. Chem. C* 112 (2008) 12769–12776.
- 103 B. Ludi, M. Niederberger, Zinc oxide nanoparticles: chemical mechanisms and classical and non-classical crystallization, *Dalton Trans.* 35 (2013) 12554–12568.
- 104 M. Huang, S. Weng, B. Wang, J. Hu, X. Fu, P. Liu, Various Facet Tunable ZnO Crystals by a Scalable Solvothermal Synthesis and Their Facet-Dependent Photocatalytic Activities, *J. Phys. Chem. C* 118 (2014) 25434–25440.

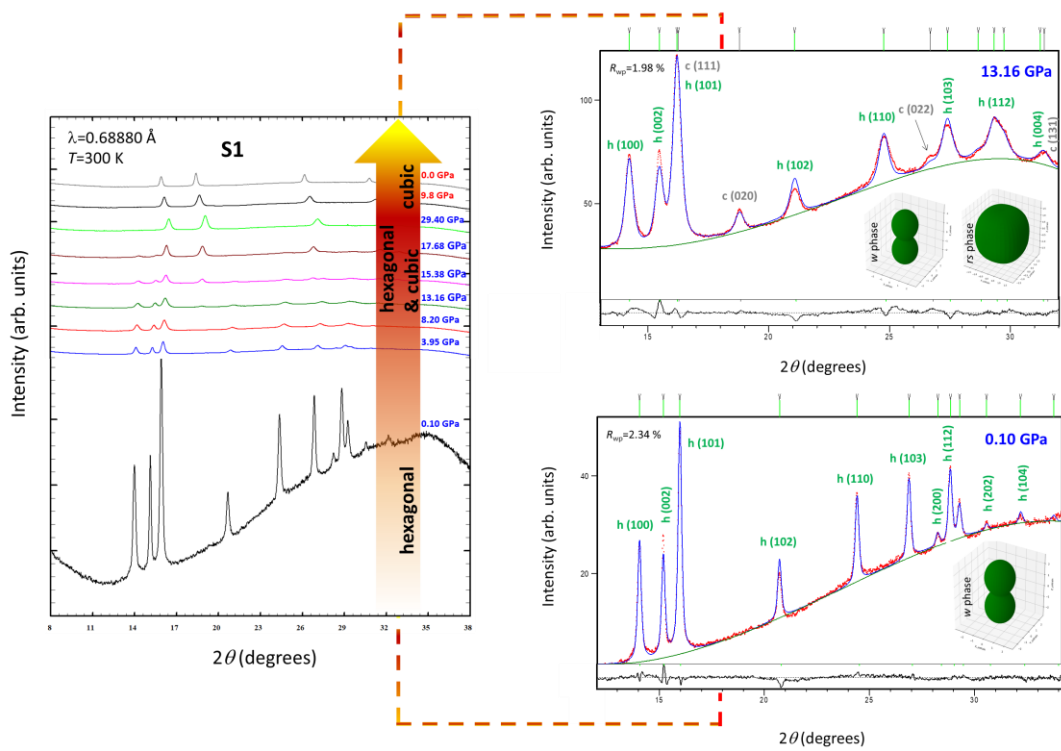
- 105 R. Saleh, N.F. Djaja, Transition-metal-doped ZnO nanoparticles: Synthesis, characterization and photocatalytic activity under UV light, *Spectrochim. Acta Part A* 130 (2014) 581–590.
- 106 C. Cheng, A. Amini, C. Zhu, Y. Xu, H. Song, N. Wang, 2014. Enhanced photocatalytic performance of TiO<sub>2</sub>-ZnO hybrid nanostructures, *Sci.Rep.*,4, 4181.
- 107 G. Kale, S. Arbu, U. Kawade, S. Rane, J. Ambekar, B.Kale, Synthesis of porous nitrogen doped zinc oxide nanostructures using a novel paper mediated template method and their photocatalytic study for dye degradation under natural sunlight, *Mater. Chem. Front.* 2 (2018) 163–170.
- 108 W. Han, L. Ren, X. Qi, Y. Liu, X. Wei, Z. Huang, J. Zhong, Synthesis of CdS/ZnO/graphene composite with high-efficiency photoelectrochemical activities under solar radiation *Appl. Surf. Sci.* 299 (2014) 12–18.
- 109 D. Chen, K. Wang, T. Ren, H. Ding, Y. Zhu, Synthesis and characterization of the ZnO/mpg-C<sub>3</sub>N<sub>4</sub> heterojunction photocatalyst with enhanced visible light photoactivity *Dalton Trans.* 43 (2014) 13105–13114.
- 110 P.S. Kumar, M. Selvakumar, P. Bhagabati, B. Bharathi, S.Karuthapandian, S. Balakumar, CdO/ZnO nanohybrids: Facile synthesis and morphologically enhanced photocatalytic performance *RSC Adv.* 4 (2014) 32977–32986.
- 111 H. T. Dao, H. Makino, Enhancement in optoelectrical properties of polycrystalline ZnO thin films by Ar plasma, *Mat. Sci. Semicon. Proc.* 96 (2019) 46–52.
- 112 L. Jing, Z. Xu, X. Sun, J. Shang, W. Cai, The Surface Properties and Photocatalytic Activities of ZnO Ultrafine Particles, *Appl. Surf. Sci.* 180 (2001) 308–314.
- 113 R. Peter, K. Salamon, A. Omerzu, J. Grenzer, I. JelovicaBadovinac, I. Šarić and M. Petravić, Role of Hydrogen-Related Defects in Photocatalytic Activity of ZnO Films Grown by Atomic Layer Deposition, *J. Phys. Chem. C*, 124, (2020) 8861–8868.
- 114 A.H. Boonstra, C.A.H.A Mutsaers, Relation between the photoadsorption of oxygen and the number of hydroxyl groups on a titanium dioxide surface, *J. Phys. Chem.* 79 (1975) 1694–1698.
- 115 Y.-H. Chin, C. Buda, M. Neurock, E. Iglesia, Reactivity of Chemisorbed Oxygen Atoms and Their Catalytic Consequences During CH<sub>4</sub>-O<sub>2</sub> Catalysis on Supported Pt Clusters, *J. Am. Chem.Soc.* 133 (2011) 15958–15978.



- 116 M. Wang, F. Zhang, X. Zhu, Z. Qi, B. Hong, J. Ding, J. Bao, J. Sun, C. Gao, Drifts Evidence for Facet-Dependent Adsorption of Gaseous Toluene on TiO<sub>2</sub> with Relative Photocatalytic Properties, *Langmuir* 31 (2015) 1730–1736.
- 117 S. Khodja, T. Touam, A. Chelouche, F. Boudjouan, D. Djouadi, Z. Hadjoub, A. Fischer, A. Boudrioua, Effects of stabilizer ratio on structural, morphological, optical and waveguide properties of ZnO nano-structured thin films by a sol–gel, *Superlattices Microstruct.* 75 (2014) 485–495.
- 118 S. Kumar, P.D. Sahare, Observation of bandgap and surface defects of ZnO nanoparticles synthesized via hydrothermal route at different reaction temperature, *Opt. Commun.* 285 (2012) 5210–5216.
- 119 B. Efafi, M. SasaniGhamsari, M.A. Aberoumand, M.H. Majles Ara, H. Hojati Rad, Highly concentrated ZnO sol with ultra-strong green emission, *Mater. Lett.* 111 (2013) 78–80.
- 120 J. Yu, X. Yu, Hydrothermal Synthesis and Photocatalytic Activity of Zinc Oxide Hollow Spheres *Environ. Sci. Technol.* 42 (2008) 4902–4907.
- 121 A.L. Stroyuk, V.V. Shvalagin, S.Y. Kuchmii, Photochemical synthesis and optical properties of binary and ternary metalsemiconductor composites based on zinc oxide nanoparticles. *J. Photochem. Photobiol. A* 173 (2005) 185–194.
- 122 M.S. Bakshi, How Surfactants Control Crystal Growth of Nanomaterials, *Cryst. Growth Des.* 16 (2016) 1104–1133.
- 123 M. Irani, T. Mohammadi, S. Mohebbi, Photocatalytic Degradation of Methylene Blue with ZnO Nanoparticles; a Joint Experimental and Theoretical Study, *J. Mex. Chem. Soc.* 60 (2016) 218–225.
- 124 R. Chaudhari, D. Landge, C.J. Bhongale, A new insight into the adsorption–dissolution growth mechanism of zinc oxide hollow hexagonal nanotowers, *RSC Adv.* 9 (2019) 20728–20732.

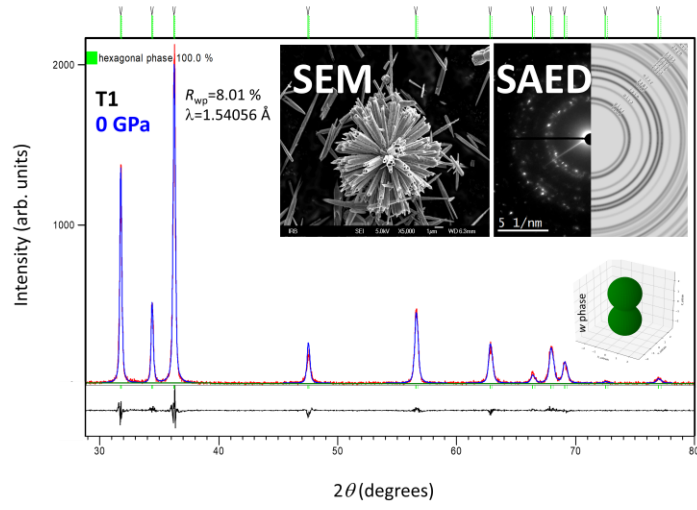


(a)

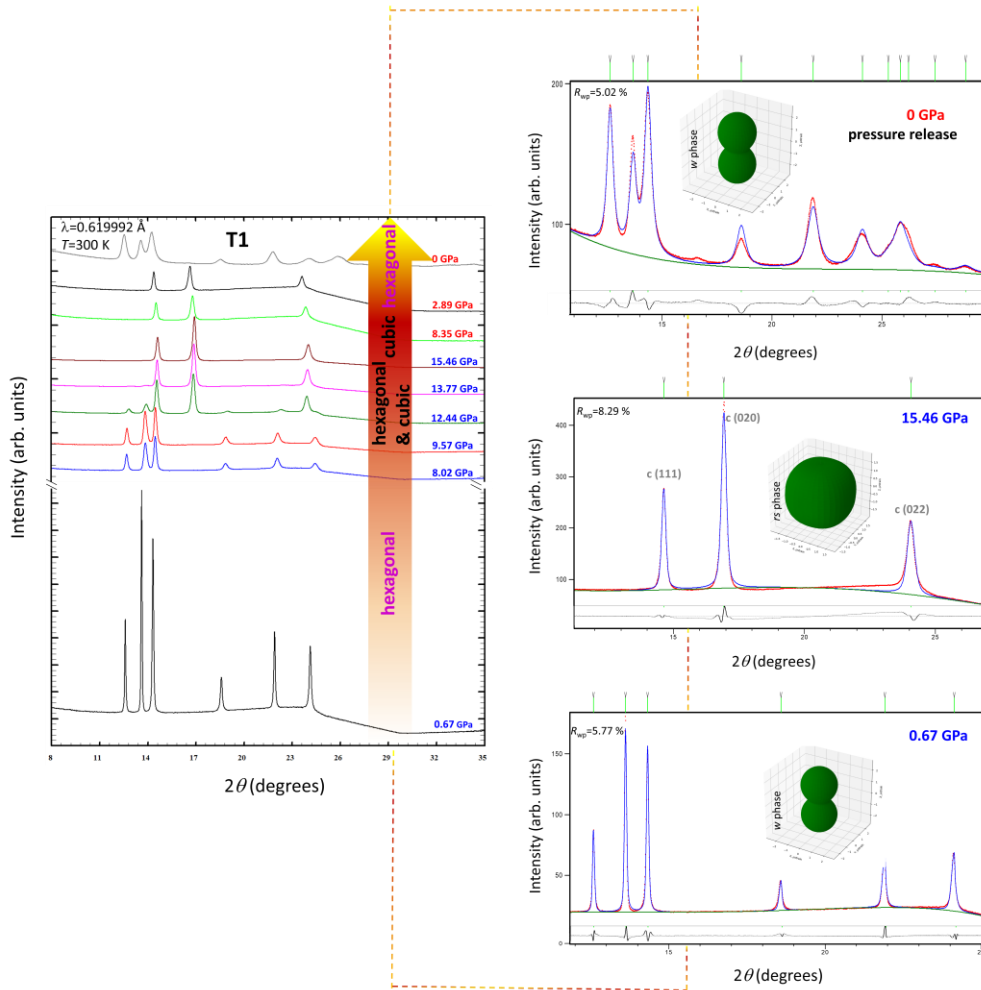


(b)

Fig. 1.



(a)



(b)

Fig. 2.

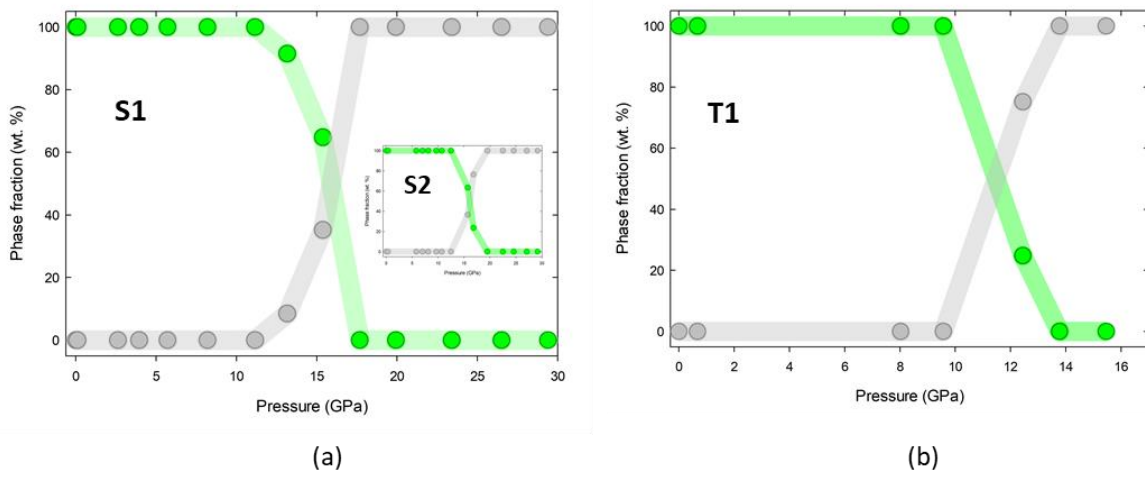


Fig. 3.

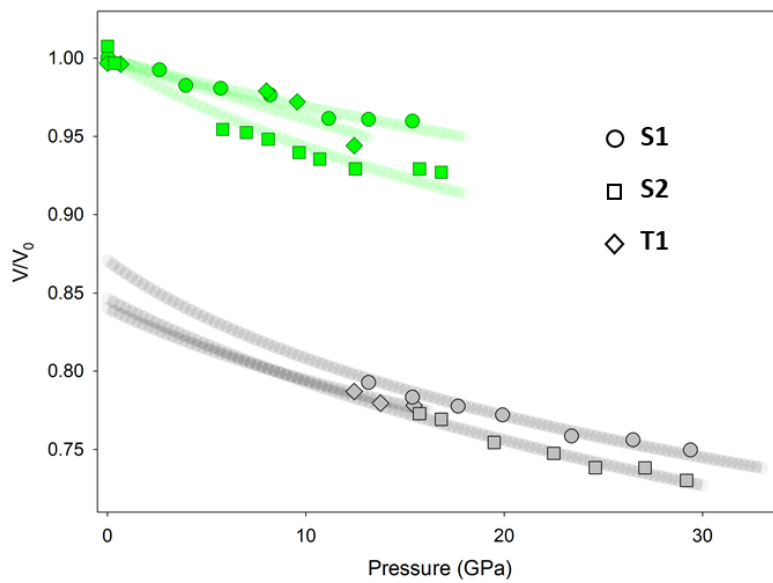
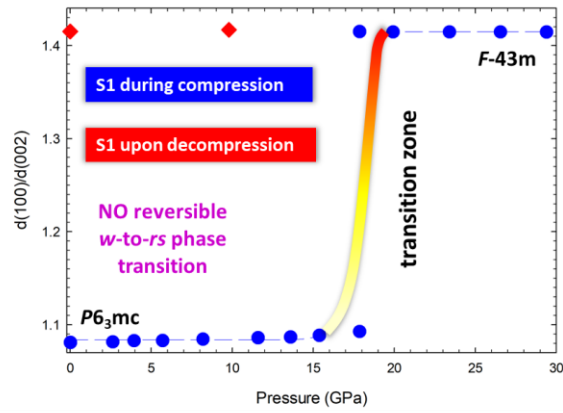
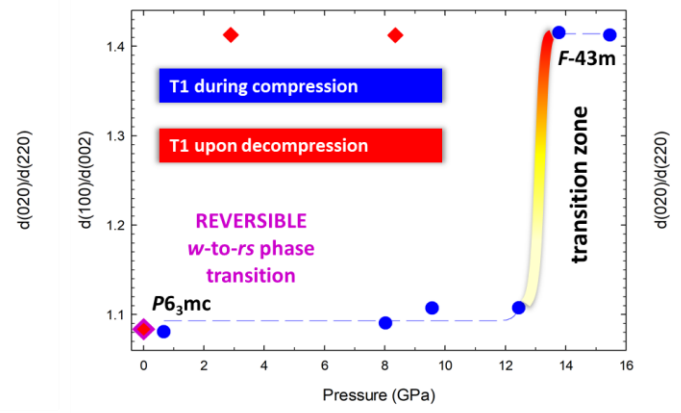


Fig. 4.

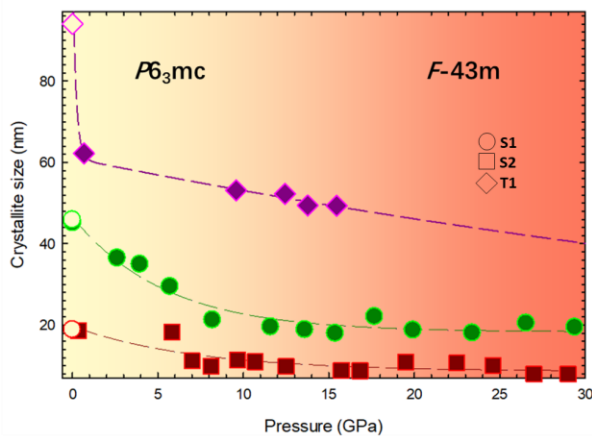


(a)

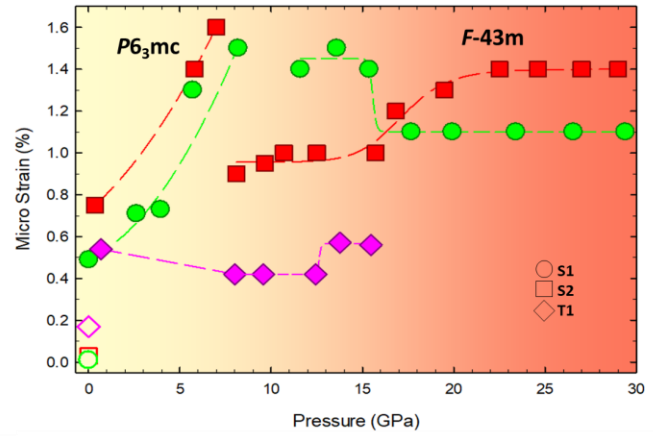


(b)

Fig. 5.



(a)



(b)

Fig. 6

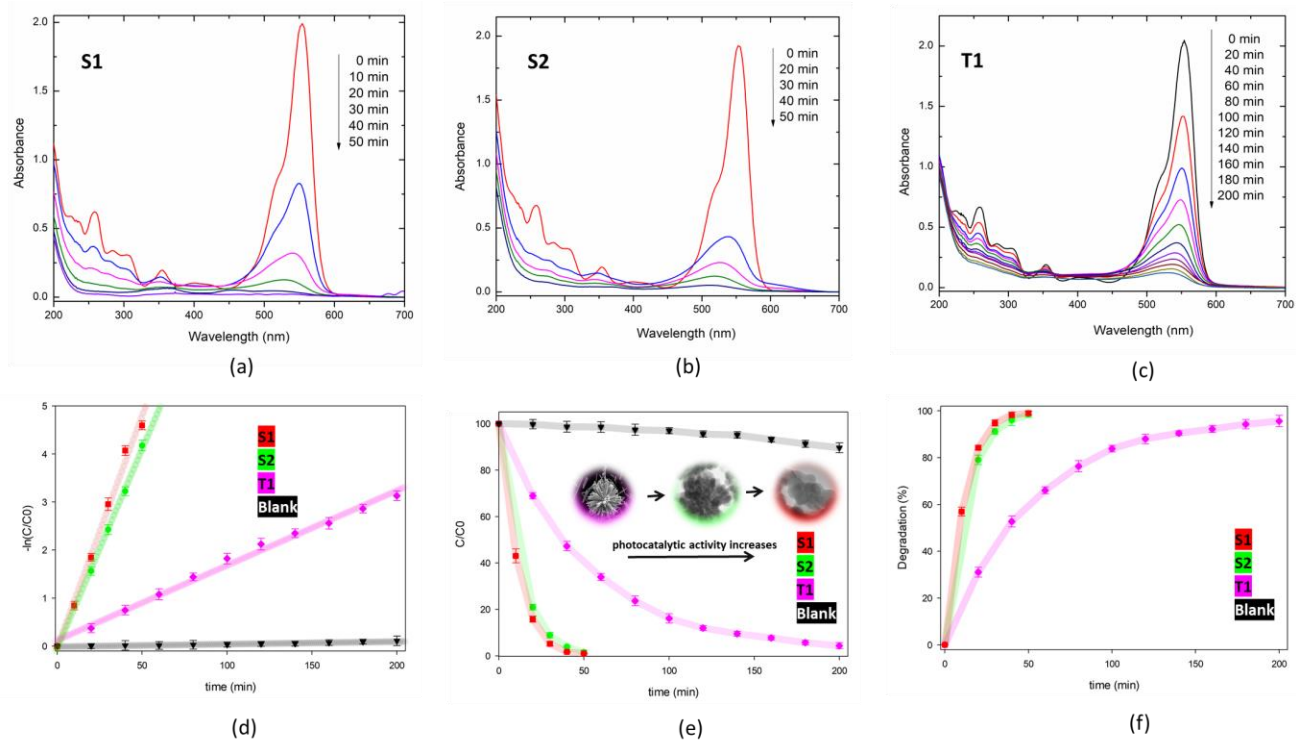


**Fig. 7**

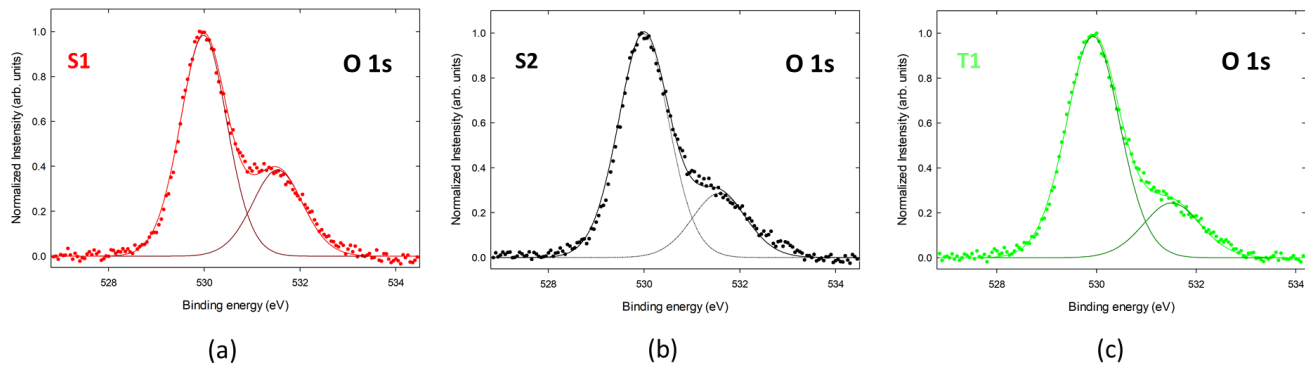


**Fig.8**

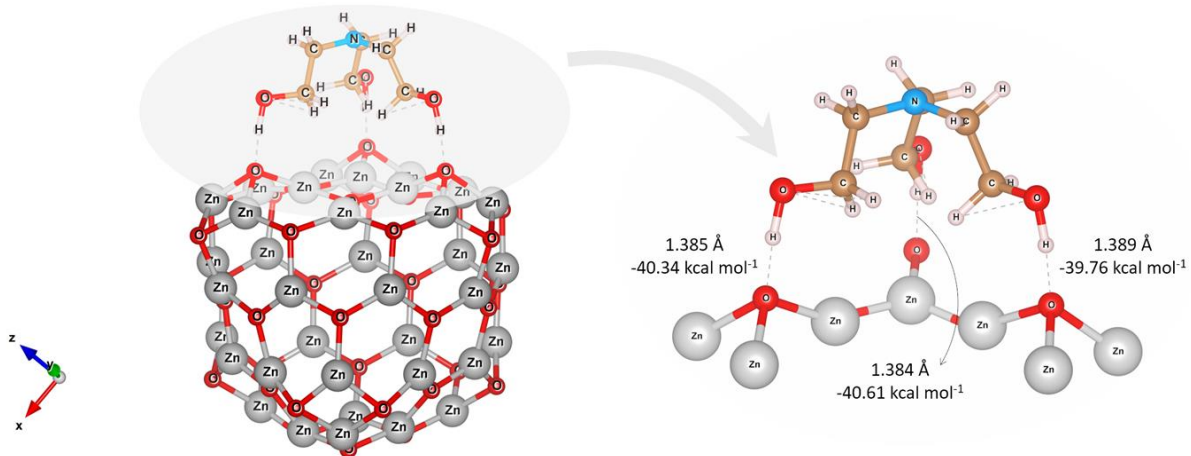


**Fig. 9.**

**Table 1.**

sample	phase	$B_0$ (GPa)	$\kappa$ (GPa <sup>-1</sup> )	$V_0$ (Å <sup>3</sup> )
S1	hexagonal	141(14)	0.0070	24.36(5)
	cubic	215(3)	0.0047	19.89(2)
S2	hexagonal	130(4)	0.0077	23.74(4)
	cubic	151(2)	0.0068	19.93(3)
T1	hexagonal	198(25)	0.0050	24.10(1)
	cubic	176(2)	0.0056	20.07(2)

**Table 2.**

sample	$R^2$	$k_{app}$ (min <sup>-1</sup> )
Blank	0.94(1)	$5(1)\times 10^{-4}$
S1	0.99(6)	$9.7(2)\times 10^{-2}$
S2	0.99(9)	$8.3(4)\times 10^{-2}$
T1	0.99(9)	$1.56(1)\times 10^{-2}$